Automated and continuous estimation of FAPAR from distributed wireless PAR sensor networks

Somnath Paramanik [a,*] , Harry Morris [b], Rémi Grousset [c], Gabriele Bai [c],
Christophe Lerebourg [c], Ernesto Lopez-Baeza [d], Ana Pérez-Hoyos [d], David Garcia-Rodriguez [e],
Darius Culvenor [f], Alexander Knohl [g], Anne Klosterhalfen [g], Frank Tiedemann [g],
Christian Lanconelli [h], Marco Clerici [i], Nadine Gobron [i], Luke A. Brown [j], Finn James [a],
Stefan Maier [k], Fabrizio Niro [l], Jadunandan Dash [a]

[a] *School of Geography and Environmental Science, University of Southampton, SO17 1BJ, Southampton, United Kingdom*
[b] *Climate and Earth Observation Group, National Physical Laboratory, Teddington, United Kingdom*
[c] *ACRI-ST, Sophia-Antipolis, France*
[d] *Albavalor, Science Park Universitat de Valencia, Paterna 46980, Spain*
[e] *University Research Institute on Robotics and Information and Communication Technologies (IRTIC), Universitat de Valencia, Paterna 46980, Spain*
[f] *Environmental Sensing Systems, Bentleigh East, Victoria, Australia*
[g] *University of Göttingen, Bioclimatology, Göttingen, Germany*
[h] *UniSystems, Milan, Italy*
[i] *European Commission, Joint Research Centre (JRC), Ispra, Italy*
[j] *School of Science, Engineering & Environment, University of Salford, Manchester M5 4WT, United Kingdom*
[k] *maitec, Darwin, Australia*
[l] *Serco for European Space Agency (ESA), Frascati, Italy*

ARTICLE INFO

ABSTRACT

Accurate estimation of the fraction of absorbed photosynthetically active radiation (FAPAR) is crucial for understanding plant productivity and ecosystem dynamics. A number of indirect measurement techniques are used for estimating FAPAR with hand-held instruments, but researchers have identified discrepancies among different techniques when using them to validate satellite land products. Many researchers have also utilised photosynthetically active radiation (PAR) sensors to obtain quantitative measurements of PAR, but these lack robust measurement frameworks and protocols. Only very limited research has started on automated wireless PAR network systems to measure at finer temporal scales as well as to reduce human error and logistical costs. This study evaluates the performance of two flux (2f) and four flux (4f) FAPAR measurement systems and digital hemispherical photography (DHP) across multiple vegetation types (e.g., vineyard, broadleaf deciduous forest, savanna woodland) and different temporal scales (instantaneous and daily integrated). Results reveal strong agreement ($R^2 > 0.99$, RMSE ≤ 0.04) between 2f- and 4f-FAPAR for all three study sites, with minimal over-estimation (bias ≤ 0.04) by the 2f systems, suggesting that it can substitute, over similar environments, the more complex and costly 4f setup without substantially compromising accuracy. Daily integrated FAPAR exhibited greater stability and lower uncertainty compared to instantaneous FAPAR, underscoring its importance for long-term ecosystem monitoring. However, instantaneous FAPAR remains essential for satellite product validation due to its alignment with satellite overpass times. Additionally, 2f-FAPAR showed a good relationship with DHP-derived FAPAR. The findings highlight the potential of the 2f wireless PAR network as an automated, cost-effective, and reliable tool for canopy light absorption studies, offering substantial advantages for both ground-based ecosystem monitoring and remote sensing applications.

* Corresponding author.
E-mail address: somnath.paramanik@soton.ac.uk (S. Paramanik).

1. Introduction

Vegetation plays a crucial role in the global energy balance, water budget, and carbon fluxes between the lower atmosphere and biosphere. Photosynthetic energy conversion utilizes incoming visible solar radiation, termed photosynthetically active radiation (PAR). The fraction of absorbed photosynthetically active radiation (FAPAR) is one of the most important biophysical variables for monitoring vegetation growth and its dynamics, and is considered an essential climate variable (ECV) by the Global Climate Observing System (GCOS) (Mõttus et al., 2012; Nightingale et al., 2018; Zemp et al., 2022). FAPAR represents the fraction of incoming solar radiation absorbed by plants in the visible spectral region (400–700 nm) (Lanconelli et al., 2024; Sellers et al., 1997; Widlowski, 2010). Long-term FAPAR observations are crucial for assessing the global carbon balance and vegetation health, serving as a critical input parameter in biogeophysical and biogeochemical-based climate and ecological models to estimate primary productivity (Gower et al., 1999; Zhang et al., 2014, 2024). FAPAR also quantifies the incoming solar radiation at the soil underlying vegetation canopies, which is crucial for the modelling of soil temperature as well as the assessment of evapotranspiration (Li et al., 2021). Furthermore, the accurate and rapid estimation of FAPAR is useful for improving crop yield estimation models, which are important for crop management (Cammalleri et al., 2022; D'Odorico et al., 2014).

FAPAR is estimated from both satellite observations and in-situ observations. On the ground, FAPAR may be derived at the point or elementary sampling unit (ESU) scale with hand-held optical instruments, such as the AccuPAR LP-80 (Meter Group, Inc., USA) and SunScan (Delta-T, Cambridge, UK) devices, which measure the downward and upward PAR fluxes at the top and bottom of the canopy via a probe containing a sensor array that is placed accordingly (Li et al., 2021; Rogers et al., 2021; Steinberg et al., 2006). Another popular method is digital hemispherical photography (DHP), from which multi-angular gap fraction may be determined with upward- or downward-facing images to estimate FAPAR. DHP images are classified based on the colour contrast between the leaves and the sky (upward) or the soil background (downward) to derive the gap fraction (Baret et al., 1993; Brown et al., 2023, 2021a, 2020a). Operating on similar principles, the LAI-2200 Plant Canopy Analyser (LICOR Inc., Lincon, Nebraska, USA) determines canopy transmittance in the blue wavelength region in five zenithal directions through above- and below-canopy measurements, from which FAPAR can be estimated (Leblanc and Chen, 2001; Li et al., 2021; Wojnowski et al., 2021).

Ground measurements are labour-intensive and pose substantial logistical challenges during field campaigns, such as the availability of well-trained operators to collect the measurements and the accessibility of the field site. Recent progress has led to the development of automated DHP systems, which acquire multiple images daily to build a temporally dense but spatially limited time-series (Brown et al., 2021c, 2020b). A remaining challenge, however, is the lack of standardized protocols that address all necessary vertical and horizontal flux measurements required for accurate FAPAR estimation (Gobron et al., 2008; Liu et al., 2025; Putzenlechner et al., 2022, 2020). Ground measurements must adequately represent the three-dimensional spatial variability of canopy attributes and radiant fluxes within the sampled domain, which is challenging to achieve consistently (Gobron et al., 2008; Lanconelli et al., 2024). These challenges collectively contribute to the complexity of obtaining accurate in-situ FAPAR measurements and highlight the need for improved measurement protocols and techniques to meet thematic uncertainty levels (0.05 units or 10 %) defined by GCOS (Roebeling et al., 2025).

Due to the challenges associated with manual in-situ measurements, researchers have recently focused on wireless sensor networks (WSNs) for measuring FAPAR with different experimental setups (Lanconelli et al., 2024; Nestola et al., 2017; Putzenlechner et al., 2019b, 2020; Widlowski, 2010). These networks offer several key advantages over traditional point-based measurements. They enable continuous, high-frequency data collection across multiple spatial locations within an ecosystem, providing a more comprehensive representation of FAPAR spatiotemporal variability (Putzenlechner et al., 2019b). This approach addresses the issue of spatial representativeness, which is crucial for accurate FAPAR estimation in heterogeneous canopies (Gobron et al., 2006; Sanchez-Azofeifa et al., 2022).

In most current protocols, FAPAR is measured by considering the flux of the solar radiation from the atmosphere, vegetation, and soil, and they are categorized (Fig. 1a) as incoming solar flux ($I_{TOC}^{\downarrow}$), flux to the ground ($I_{BOC}^{\downarrow}$), flux from the ground ($I_{BOC}^{\uparrow}$), outgoing solar flux ($I_{TOC}^{\uparrow}$) (Gobron et al., 2006; Liang and Wang, 2020). Based on the number of flux terms (n) being measured, they are termed as n-flux FAPAR systems. The four flux FAPAR (4f-FAPAR) considers all the vertical fluxes of up- and down-welling radiation at the top-of-canopy (TOC) and bottom-of-canopy (BOC) levels, whereas the two flux FAPAR (2f-FAPAR) ignores the up-welling radiation contribution at the BOC and TOC (Fig. 1b). Long-term deployment of WSNs facilitates the capture of phenological effects and seasonal variations in FAPAR, enhancing our understanding of vegetation dynamics (Fensholt et al., 2004; Lee et al., 2023). The automation aspect also reduces human error and allows for data collection under various environmental conditions, improving the consistency and reliability of measurements (Camacho et al., 2013; Vedurmudi et al., 2025; Wang et al., 2016). While the initial implementation of such networks may be resource-intensive, they offer a robust solution for obtaining high-quality, consistent FAPAR data across diverse ecosystems, ultimately improving the validation of satellite-derived FAPAR products and enhancing our ability to model terrestrial carbon dynamics (Camacho et al., 2024; McCallum et al., 2010; Xia et al., 2025; Xiao et al., 2015) .

Long-term FAPAR observations are required to understand terrestrial carbon dynamics (forest biomass, crop yield) and the effects of global climate change, which is only feasible by developing satellite-based FAPAR products on regional as well as global scales (Xiao et al., 2018). Multiple global FAPAR products from different sensors (e.g., Advanced Very High Resolution Radiometer (AVHRR), Moderate Resolution Imaging Spectroradiometer (MODIS), Medium Resolution Imaging Spectrometer (MERIS), Satellite Pour l'Observation de la Terre (SPOT) VEGETATION, Project for On-Board Autonomy – Vegetation (PROBA-V), Sentinel-3 Ocean and Land Colour Instrument (OLCI)) have been developed (Camacho et al., 2013; Gobron et al., 2022; Myneni et al., 2002; Origo, 2023; Zhang et al., 2024; Zheng et al., 2022; Zhu et al., 2013). These products rely on empirical relationships with vegetation indices or inversion of canopy radiative transfer models (Lanconelli et al., 2024; Xiao et al., 2018; Zhang et al., 2024, 2025). Though most FAPAR products depict a similar seasonal pattern (D'Odorico et al., 2014; Gobron et al., 2007), intercomparisons among FAPAR products from multiple satellite sensors (MODIS, SEVIRI, MERIS) reported discrepancies in the magnitude of the FAPAR values. Among all the biome types, broadleaf and needleleaf forest showed substantial disagreement (Martínez et al., 2013). Many studies (Brown et al., 2021a, 2020a; Pickett-Heaps et al., 2014; Zheng et al., 2022) evaluated these global satellite products with in-situ measurements, which revealed inconsistency. Furthermore, research also demonstrated that global FAPAR products (MISR, MODIS, MERIS, GEOV1) did not meet the recommended uncertainty (0.05) by GCOS (Tao et al., 2015).

The available ground measurements for FAPAR product validation are mostly in forest ecosystems and rely on indirect measurement techniques such as DHP (Brown et al., 2020a; Fernandes et al., 2023; Nestola et al., 2017), which may add uncertainty due to approximations and assumptions associated with image collection and processing. Though there are potential advantages associated with WSNs, relatively few studies have focused on them (Origo, 2023; Putzenlechner et al., 2019b, 2020; Sanchez-Azofeifa et al., 2022) to estimate in-situ FAPAR and their evaluation. Direct FAPAR measurements tend to lack sufficient
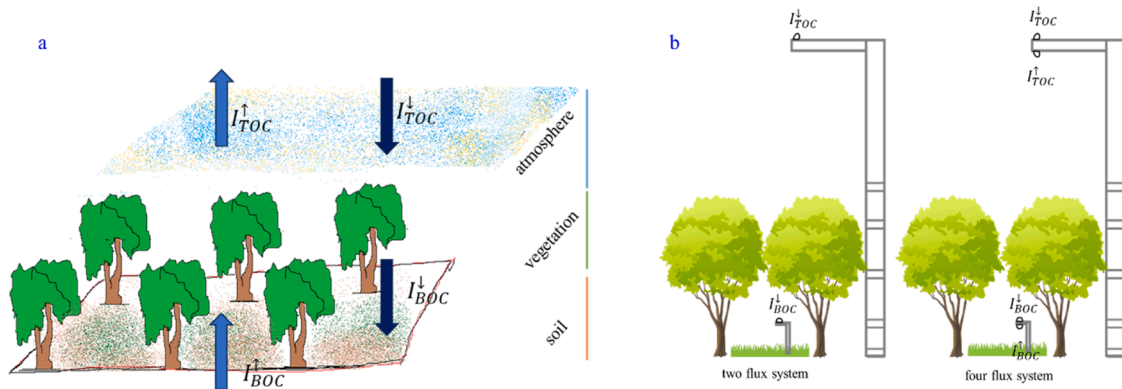
Fig. 1. (a) schematic diagram of flux budget, which is adapted from Liang and Wang (2020); (b) schematic diagram of 2f- and 4f-PAR measurement systems.

samples due to the limited availability of PAR sensors, which hinders accurate representation of spatial as well as temporal variability across diverse vegetation ecosystems. In this study, we developed and tested an FAPAR estimation framework at three continuous long-term ground observatory sites belonging to the Ground-Based Observations for Validation (GBOV) initiative. GBOV is used to validate seven core satellite land products (top-of-canopy reflectance, surface albedo, FAPAR, leaf area index, the fraction of vegetation cover, land surface temperature, and soil moisture) (Bai et al., 2022; Brown et al., 2021b), and is maintained by the Copernicus Land Monitoring Service (https://gbov.land.copernicus.eu/). A wide range of studies have used GBOV data to evaluate satellite land products (Brown et al., 2020a; Li et al., 2023; Lin et al., 2023; Pu et al., 2023; Sánchez-Zapero et al., 2023; Wan et al., 2024; Yan et al., 2025; Zhao et al., 2024).

Although 'Component 1′ of GBOV mostly reliant on data provided by existing environmental monitoring networks, 'Component 2' has focused on equipping and upgrading additional sites with automated instruments, ensuring the provision of long-term, robust validation datasets to achieve CEOS recommendations (Lerebourg et al., 2024; Niro et al., 2021). GBOV is also adopting the uncertainty evaluation framework developed in the European Space Agency (ESA) Fiducial Reference Measurements for Vegetation (FRM4VEG) project (Brown et al., 2021a; Camacho et al., 2024) (https://frm4veg.org/). Combined, these will represent a rich resource of reference data for future satellite data validation. While WSNs have shown potential for validating satellite-derived FAPAR products, their application for systematically comparing multiple flux-based estimation schemes across diverse ecosystems with multi-temporal data remains relatively underexplored. Furthermore, clear protocols and guidelines for selecting the optimal number of fluxes and assessing uncertainties associated with different measurement approaches are currently lacking.

This study aims to address these gaps by evaluating the consistency between 2f- and 4f-FAPAR measurements across three distinct ecosystems: an agricultural vineyard, a natural deciduous forest, and a savanna woodland. The study also assesses the impact of quality control (QC) procedures on the recorded PAR dataset and compares daily integrated (sunrise to sunset) and instantaneous (satellite overpass) FAPAR estimates. WSNs-measured FAPAR is intercompared with DHP-derived FAPAR. The findings of this study will contribute to establishing practical guidelines for selecting the most appropriate FAPAR estimation scheme based on specific field conditions and will ultimately improve the accuracy and reliability of ground-based FAPAR measurements, which are crucial for validating and refining satellite-derived FAPAR products.

2. Materials and methods

2.1. Study sites

2.1.1. Valencia anchor station

The Valencia Anchor Station (VAS) is located (Latitude: 39.5712, Longitude: −1.2848) in the Utiel-Requena Plateau, approximately 80 km west of the city of Valencia, Spain. The University of Valencia set up the VAS, with operations commencing on 1st January 2002. The area is intensively used for agriculture, predominantly for wine (*Vitis vinifera*) growing, but there are also substantial olive (*Olea europaea*) and almond (*Prunus dulcis*) plantations. Ridges are often covered by pines (*Pinus* spp.) and a characteristic form of shrubland (matorral). Outside the vineyard growing season, VAS remains mostly under bare soil conditions (Fig. 2a). The topography is predominantly flat (slope < 2 %), and the climate is classified as dry-sub-humid (Carbó et al., 2021; López-Baeza et al., 2003), with average annual precipitation of approximately 450 mm. In February 2020, the PAR WSNs (Fig. 2b) were installed in VAS. The site has previously been used for an ESA-funded in-situ field campaign for the validation of the Sentinel-3 Ocean and Land Colour Instrument (OLCI) Terrestrial Chlorophyll Index (OTCI) in 2017 (Brown et al., 2019).

#### 2.1.2. Hainich national park

The Hainich National Park (HNP) is part of a transboundary UNESCO world heritage site. The study site is located (Latitude: 51.0790, Longitude: 10.4507) within the national park approximately 15 km north-east of the city of Eisenach, Germany at 439 m above sea level. The national park was established in 1997 to protect one of Central Europe's largest (7600 ha) beech forests. The study site was established in 1999 and is currently managed by the University of Göttingen. The HNP consists of an unmanaged mixed deciduous forest dominated by European beech (*Fagus sylvatica* L.) and scattered deciduous broadleaf species such as ash (*Fraxinus excelsior* L.) and maple

(*Acer* spp.), where the trees cover a wide range of age classes, with a maximum age of up to 265 years, with a mean age of all trees of 140 years (Tamrakar et al., 2018). Maximum tree height varies in the range between 30 m and 35 m (Fig. 2d), with a maximum leaf area index of 5.1, and the tree density is 334 trees/ha. The mean annual temperature and precipitation is 6.8 °C and 872 mm (Heidenreich and Seidel, 2022; Knohl et al., 2003). The HNP site is part of the Integrated Carbon Observation System (ICOS) network (DE-Hai; https://www.icos-cp.eu/) and measures both meteorological as well as ecosystem variables (Gielen et al., 2018; Kloos et al., 2024). Under GBOV, an automated DHP system (Fig. 2g) is also installed for routine canopy monitoring (Brown et al., 2021c).

2.1.3. Litchfield savanna supersite

The Litchfield Savanna SuperSite (LSS) is located (Latitude:
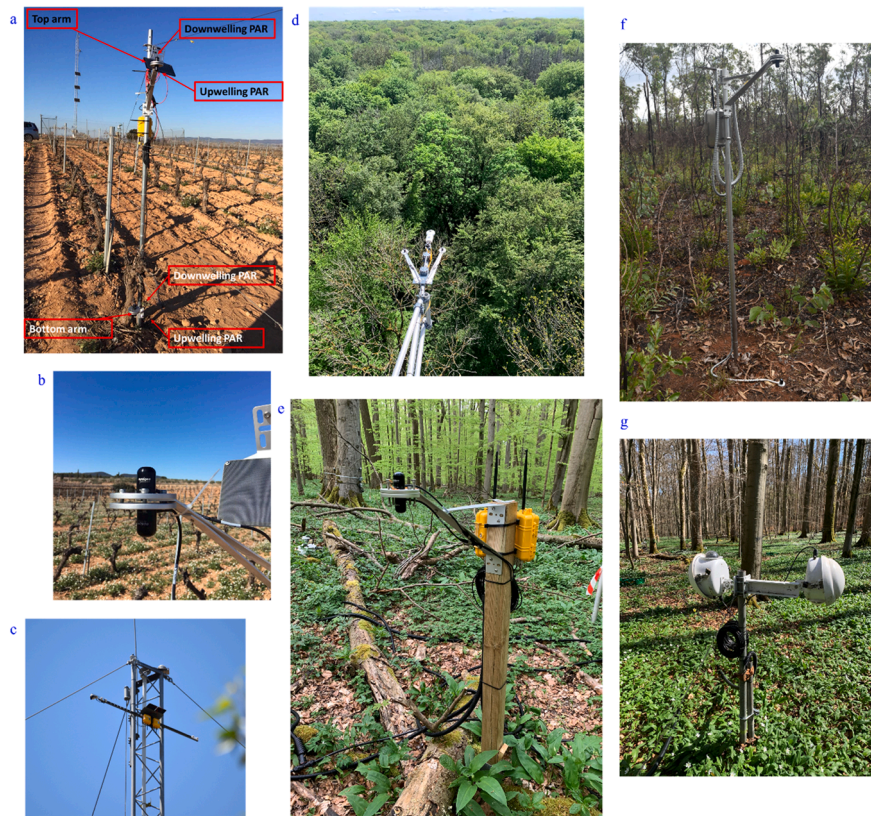
Fig. 2. (a) the sensor nodes were fixed at VAS in both rows as well as in between rows, where in each node four sensors were installed for capturing upwelling and downwelling PAR; (b) Apogee PAR sensors were set up for the measurements; sensors are installed at the top of the tower in LSS (c) as well as in HNP (d) for measuring the PAR fluxes at TOC; for measuring the PAR fluxes at BOC, sensors are installed in both forest sites HNP (e) and LSS (f); the automated DHP system (g) was installed in HNP.

−13.1791, Longitude: 130.7943, approximately 80 km south of Darwin, Northern Territory, Australia. The LSS is a component of Australia's national vegetation monitoring network, known as the Terrestrial Ecosystem Research Network (TERN) (https://portal.tern.org.au/browse/theme) (Cleverly et al., 2019; Karan et al., 2016). TERN was founded in 2009 and collects a wide variety of data, including soil properties, vegetation characteristics, ecosystem fluxes, climate, biodiversity, and remote sensing data (Karan et al., 2016). The site consists of mesic tropical savanna woodland, where overstorey tree species are dominated by *Eucalyptus miniata, Eucalyptus tetrodonta,* and *Eucalyptus latifolia,* with a mean height of 18 m and stand density of 700 stems per ha. The site has a tropical climate with an average maximum temperature of 32 °C and a mean annual precipitation of 1890 mm (D'hont et al., 2021), with 90 % of precipitation occurring between October and April. Wildfires have frequently burned the LSS over the last 20 years, and fires mostly occur from May to September (dry season) due to the accumulation of fuel loads.

2.2. Sampling designs for PAR measurements

The sampling designs varied based on the ground conditions and vegetation type. For PAR data collection within an ESU, strategically, a distinct number of nodes is positioned. Each node represents a single stand that holds multiple PAR sensors to capture the upwelling and downwelling radiation. Inside the ESU, they are termed as nodes, and outside of the ESU, they are termed as the tower. Table 1 provides an overview of the data sampling design at the three sites.

At the VAS, each node contains four PAR sensors (Fig. 2a) to measure the four fluxes needed to calculate FAPAR. Two different types of nodes are defined: those within-vines and those between-vines. These are arranged crosswise within the ESU (Fig. 3a). The PAR nodes between the

Table 1
Sampling protocols for PAR and DHP measurements.

	Valencia Anchor Station (VAS)	Hanich National Park (HNP)	Litchfield Savanna SuperSite (LSS)
Approximate ESU size	60 *m* × 60 m	50 m x 50 m	50 *m* × 50 m
Number of sensor nodes in each ESU	12	14 (4 below and above understorey, 8 above understorey, 1 tower, 1 bare soil)	12 (3 below and above understorey, 6 above understorey only, 2 tower, 1 bare soil)
Temporal frequency of data	Measured every 5 min	Measured every 5 min	Measured every 5 min
Height of the PAR sensor nodes/towers	1.8 m, and 0.2 m	43 m	31 m
DHP data	Manual field campaign	Automated system	
DHP location	Between and within rows	Centre of the ESU	
DHP camera, lens specification	Canon EOS 80D and Sigma 4.5 mm F2.8 EX DC fisheye lens	Canon EOS 1300D and Sigma 4.5 mm F2.8 EX DC fisheye lens	
PAR Quantum sensors	Apogee SQ-110-SS	Apogee SQ-110-SS	Apogee SQ-110-SS

two rows and on the rows are maintained at a 15 m spacing. This representative arrangement (on row and between the rows) of the PAR sensor nodes was designed with the aim of reducing the bias of
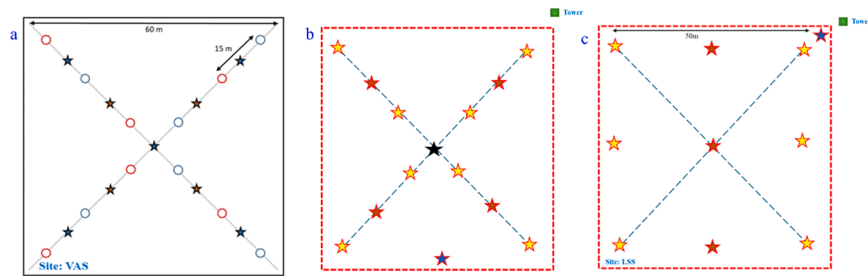
Fig. 3. ESU architecture design of three sites: VAS (a), the blue circles represent the PAR nodes between the two rows of the vineyard, whereas the red circles represent the PAR sensor nodes on the rows. The blue stars represent the DHP measurements between rows, and the red stars represent the DHP measurements on rows; HNP (b), the red stars on the diagram are composed of one node for each kind of node, and the yellow stars are composed solely of the above lower canopy node. The black star represents the automated DHP system, and the blue star is an above lower canopy node put in place without vegetation to measure the PAR on bare soil and litter layer, but they have not been used in the data analysis; LSS (c), the red, yellow, and blue stars are representing the same purpose of sensing as HNP.

measurements and maintaining the interception heterogeneity of incoming and outgoing fluxes. The ESU size of the VAS is 60 m × 60 m. The base station is situated to the north of the sampling nodes, approximately 120 m away from the furthest node.

At the HNP site, outgoing and incoming solar fluxes are measured using two nodes on a flux tower outside of the ESU (Fig. 3b), to measure the fluxes above the canopy at a height of 43 m (Fig. 2d). The other nodes are composed of two PAR sensors, either on the ground measuring the flux to the ground or above the lower canopy (Fig. 1m) measuring the flux to the ground and the flux from the ground. Below the canopy (Fig. 2e), twelve nodes were arranged in a cross-shaped pattern (three nodes per arm), which are responsible for overstorey FAPAR estimation. At the ground level, four nodes are positioned directly on the soil surface (each node with two sensors looking up), which are responsible for the understorey FAPAR estimation. Finally, one bare-soil node is placed at 40 cm above the soil surface (one sensor looking up and one looking down). This bare-soil node and four soil surface nodes have not been used in this current study, as overstorey FAPAR estimation is the recent focus (Fig. 2c and d).

At LSS, outgoing and incoming solar fluxes are also measured with two nodes composed of two PAR sensors located on a flux tower (Fig. 2c) above the canopy, as well as six above the understory measuring nodes (Fig. 2f). As in HNP, there is a bare soil node outside of the ESU, and inside the ESU, there are two kinds of nodes. The first kind is the same above the lower canopy as in HNP, and the second is an above lower canopy node with one more PAR sensor put on the ground measuring the flux to the ground. The nodes are arranged in a three-by-three matrix; the ESU (Fig. 3c) size of the LSS is 50 m × 50 m. Along with the sensor node, the data logger was also set to store and transfer the measurements.

2.3. Electronic device

The PAR sensor used at each site is the Apogee model SQ-110-SS calibrated for operation in sunlight, which is arranged in nodes containing two, three, or four sensors, depending on the site. One PAR sensor might measure either the incoming solar flux, the outgoing solar flux, the flux to the ground, or the flux from the ground. The sensors are sensitive to wavelengths between 410 - 655 nm and produce an analogue voltage that is directly proportional to photosynthetic photon flux in units of micromoles per square meter per second (μmol m^{-2} s^{-1}). The nodes consist of PAR sensors, a solar charging circuit designed to charge a single-cell LiFePO4 battery that powers the entire electronic system, and a wireless datalogger featuring a LoRaWAN and Wi-Fi enabled microcontroller. The microcontroller acquires sensor data and facilitates wireless data transfer to a local base station using both Wi-Fi and LoRaWAN communication protocols Each node includes an on-board real-time clock (RTC) based on a DS3231 device with internal temperature compensation and accuracy of ±2 ppm from 0 °C to +40

°C. System time is initially set and subsequently maintained using a Network Time Protocol (NTP) server over Wi-Fi. Sensor data were measured using a 16-bit analogue-to-digital converter (ADC) with 4x gain (1 bit = 0.03125 mV). Final recorded values were derived from the average of fifty samples over a period of 1 s for each sensor channel. Measurements were interlaced across all ADC channels (2 or 4, depending on flux inputs) during the 50 samples to ensure any illumination variation was captured consistently during the 1 s measurement period.

2.4. DHP data collection

In VAS, DHP images were collected in multiple manual field campaigns over the ESU scale. Upward-facing DHP measurements were obtained across the growing season, covering the same plot as the FAPAR network. A Canon digital single lens reflex (DSLR) EOS 80D camera equipped with a Sigma 4.5 mm F2.8 EX DC fisheye lens was used to acquire twenty-one upwards-facing images across the two transects of the ESU (Fig. 3a). In HNP, an automated DHP system was installed, which includes a Canon DSLR, EOS 1300D camera equipped with a Sigma 4.5 mm F2.8 EX DC fisheye lens. This automated DHP system consists of two modified Harbortronics Cyclapse time-lapse cameras, each with a waterproof housing, acrylic dome, and a DigiSnap Pro intervalometer. The set of cameras was mounted at the centre of the ESU (Fig. 3b) at 1.3 m above ground, collecting raw images every 30 min between 05:00 and 21:00 local time (Brown et al., 2021c).

2.5. Methodology

The adopted FAPAR estimation framework follows multiple steps (Fig. 4), including i) sensor setup in selected (GBOV) sites, ii) data collection through the electronic network and data logger, and finally, iii) processing of the data. In this study, we focus on the development of the data processing steps. Datasets obtained for three sites are analysed: VAS (from 02/02/2021 to 29/11/2024), HNP (from 13/04/2023 to 29/11/2024), and LSS (from 05/12/2021 to 03/06/2024). In our analysis, we compared 2f- and 4f-FAPAR considering two-time frames (e.g.,
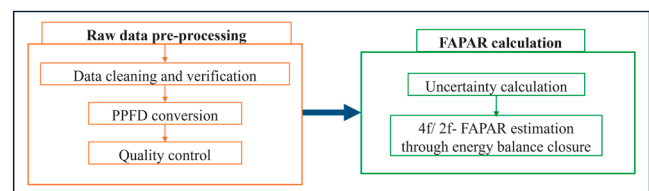
Fig. 4. The processing steps followed to estimate 2f- and 4f-FAPAR from WSNs. WSNs-derived FAPAR estimation processes are divided into two broad steps: raw data pre-processing (orange box) and FAPAR calculation (green box).

instantaneous and daily integrated). Finally, the 2f-FAPAR approach was compared with DHP-derived FAPAR.

2.5.1. Raw data pre-processing

Data from the PAR sensor networks, recorded as analogue-to-digital converter (ADC) output, were acquired from the GBOV data archive. A pre-processing chain was implemented to ensure data quality and continuity. Invalid data files were excluded from the analysis by identifying errors in the data structure (e.g., data repetition for the same timestamp, misposition or shifting of the columns, etc.). To ensure synchronization across all the sensor nodes, timestamps were rounded to a common 5-minute interval to account for internal clock drift. The adopted data loggers within each node stored the intensity of the incoming radiation as a 16-bit value. This input signal could then be converted to photosynthetic photon flux density (PPFD) in units of micromoles per square meter per second (μmol m^{-2}s^{-1}) as

$$PPFD = ADC \times 0.03125 \times 5 \; \mu mol \; m^{-2}s^{-1} \tag{1}$$

where ADC is given in mV, 0.03125 is the programmable gain factor, and 5 is the nominal factory calibration in $\mu mol m^{-2}s^{-1}$ per mV.

To ensure the reliability and accuracy of the data, several quality control (QC) steps were applied to the PPFD outputs of each sensor, focusing on physical validity, sky-condition filtering, and statistical outlier detection.

2.5.1.1. Basic QC, time sync, and slicing.
Initially, the first and basic QC step was the removal of values that were less than or equal to zero from the measurements. The value of zero suggests the sensor is off or blocked, while a negative value indicates an electrical circuit fault or a sensor miscalibration. Based on the requirement of the timeframe (e.g., instantaneous and daily integrated), datasets were sliced. To derive instantaneous FAPAR, PAR measurements were restricted to 10:00 local solar time ($\pm$ 15 min). Meanwhile, daily integrated FAPAR was calculated by averaging the PAR measurements from sunrise to sunset based on the solar zenith angle (Θ_s). This step also ensures timestamp synchronization among sensor nodes for all fluxes.

2.5.1.2. Physical validity based on energy conservation.
First, several constraints were implemented to maintain physical validity in the radiation flux calculations for the computation of 2f- and 4f-FAPAR. These constraints ensure FAPAR values are physically plausible (i.e., between 0 and 1). For the 4f-systems, this included ensuring consistency between upward and downward fluxes and an energy balance (Eq. (2)) constraint to ensure that the energy absorbed by the canopy was not greater than the incident energy. For the 2f-systems, constraints were applied to ensure non-zero incident radiation and dominant incident radiation (Eq. (3)). The flux values that did not meet these criteria were flagged and excluded from the dataset (Long and Shi, 2008; Pashiardis et al., 2023).

$$I^{\downarrow}_{TOC} > I^{\downarrow}_{BOC}, \; I^{\downarrow}_{TOC} > I^{\uparrow}_{BOC}, \; I^{\downarrow}_{TOC} > I^{\uparrow}_{TOC} \tag{2}$$

$$I^{\downarrow}_{TOC} > 0, \; if \; I^{\downarrow}_{TOC} = 0 \; then \; I^{\downarrow}_{BOC} \; must \; also \; be \; 0 \tag{3}$$

2.5.1.3. clouds and associated flags.
The physical integrity of the PAR measurements was ensured through a series of rigorous radiometric QC checks to minimize erroneous data. We removed all data points pertaining to Θ_s higher than 80° (Lozano et al., 2023a). This step is crucial as measurements taken at low sun angles are highly susceptible to the cosine response error of the diffuser. The geometric normalisation factor itself concerns instrument levelling, minor uncertainty related to imprecise calculations of the sun zenith angle over geometric ranges where the assumptions of parallel atmosphere may become weak, and refraction that should be accounted for explicitly. Following this, the clearness index (K_t) was calculated as the ratio between the measured incoming $I^{\downarrow}_{TOC}$ to the theoretical extraterrestrial PAR (G_0) for the given

time and location (Lozano et al., 2023a), as follows:

$$K_t = I^{\downarrow}_{TOC} / G_0 \tag{4}$$

$$G_0 = G_{sc}\mu_0 E_0 \tag{5}$$

where, G_{sc} is the solar constant for the PAR range, which is 531.8 Wm^{-2} or 2430.33 $\mu mol \; m^{-2}s^{-1}$, as the 'quanta to energy' ratio is considered here as 4.57 $\mu mol \; J^{-1}$ (Gueymard, 2018), E_0 is the eccentricity correction factor, which is calculated by means of approximated parameterization (Duffie and Beckman, 2013; Iqbal, 1983; Yu et al., 2015) as

$$E_0 = 1 + 0.033 \times cos\left(\frac{360 \times n}{365}\right) \tag{6}$$

being n is the Julian day of the year, and μ_0 is the cosine of the Θ_s.

In our analysis, data points where K_t were outside the physically possible range of 0 to 1 were flagged and removed. High values of K_t indicate clear-sky conditions or thin clouds (subvisible and cirrus clouds), whereas lower values of K_t indicate the presence of thick clouds and fog (supplementary-S1). Intermediate values are often related to scattered clouds (Duchon and O'Malley, 1999).

Before further processing, to avoid outliers and extreme values, we used the 1st and 99th percentiles to define the acceptable data range (Lozano et al., 2023a). These QC steps ensured the dataset's integrity, enabling robust estimation of FAPAR from PAR flux measurements:

$$K_t \; is \; valid \Leftrightarrow (\Theta_s \in B_i) \; and \; (P_{L,i} \leq K_t \leq P_{U,i}) \tag{7}$$

where B_i is a specific zenith angle bin (for our analysis, we segregated every 10°), $P_{L,i}$ is the lower percentile (e.g., 1st percentile), and $P_{U,i}$ is the upper percentile (e.g., 99th percentile).

After applying all the robust QC processes, a significant portion of the initial dataset was filtered (supplementary-S2) to ensure data integrity: 739,157 rows (VAS), 227,845 rows (HNP), 455,041 rows (LSS) were found as valid data for further FAPAR estimation.

2.5.2. FAPAR calculation

After pre-processing and quality control, the developed framework for estimating FAPAR was utilized. This process generated 2f- and 4f-FAPAR values, along with their corresponding uncertainties, and involved the following steps.

2.5.2.1. Uncertainty calculation.
To generate in-situ datasets that are suitable for validating satellite data products, it is paramount that reference measurements include an associated uncertainty. To quantify the uncertainty in the 2f- and 4f-FAPAR values derived from the WSNs, FRM4VEG recommendations (Brown et al., 2021a) were followed. This involved the identification of relevant uncertainty components and the quantification of these components, which were then combined using the law of propagation of uncertainty. This approach is in accordance with the Bureau International des Poids et Mesures (BIPM) Guide to the Expression of Uncertainty in Measurement (GUM), distributed by the International Standards Organisation (ISO).

The uncertainty associated with the PAR measurements provided by the Apogee SQ-110-SS sensors arises from two main sources. Firstly, uncertainties are associated with the sensors themselves, including calibration (u_{cal}), repeatability (u_{rep}), long-term drift (u_{drift}), directional errors (u_{dir}), non-linearity (u_{lin}), and temperature sensitivity (u_{temp}) uncertainties. Additionally, there are uncertainties associated with the conditions under which measurements were made, such as those associated with imperfect instrument leveling (u_{lev}) (Origo et al., 2017), dust, and bird droppings (Harris et al., 2025; L. Liu et al., 2024). Individual uncertainty components were first identified, and the combined standard uncertainty in each sensor's PPFD measurements was then calculated by adding these uncertainty components in quadrature. Mathematically, this can be expressed as

$$u_{PPFD} = \sqrt{u_{cal}^2 + u_{rep}^2 + u_{drift}^2 + u_{dir}^2 + u_{lin}^2 + u_{temp}^2 + u_{lev}^2} \qquad (8)$$

Table 2 presents each uncertainty component. In the absence of primary calibration and characterization data, these components were quantified using 'Type B' evaluation (e.g. manufacturer's specifications and previously published information) to provide a first-order approximation. The uncertainty associated with the PPFD values for each sensor was propagated through the calculation of 2f- and 4f-FAPAR according to the law of propagation of uncertainty.

2.5.2.2. 4f- and 2f-FAPAR estimation through energy balance closure. The 4f-FAPAR system estimates the canopy absorption by considering all the vertical fluxes of up and down-welling radiation at TOC and BOC levels and assumes horizontal fluxes are negligible. The 2f-FAPAR also ignores the up-welling radiation contribution at the BOC and TOC. Their explicit definitions are

$$FAPAR_{4f} = \frac{I_{TOC}^{\downarrow} - I_{BOC}^{\downarrow} + I_{BOC}^{\uparrow} - I_{TOC}^{\uparrow}}{I_{TOC}^{\downarrow}} \qquad (9)$$

$$FAPAR_{2f} = 1 - \frac{I_{BOC}^{\downarrow}}{I_{TOC}^{\downarrow}} \qquad (10)$$

where $I_{TOC}^{\downarrow}$: incoming solar flux; $I_{BOC}^{\downarrow}$: flux to the ground; $I_{BOC}^{\uparrow}$: flux from the ground; and $I_{TOC}^{\uparrow}$: outgoing solar flux from TOC.

As the measurement systems were designed for measuring ESU scale FAPAR, each flux was averaged over all nodes within the ESU, enabling FAPAR to be computed at the ESU scale (i.e., as opposed to averaging FAPAR computed individually for each node).

2.5.3. DHP-based FAPAR estimation

At the VAS site, DHP data were collected during periodic field campaigns, whereas at HNP, they were collected using automated DHP systems (Brown et al., 2021b, 2020a). The automated system collected DHPs, which were converted to daily measurements by using a weighted average that depends on the solar zenith angle. Before the estimation of FAPAR from the DHP data, QC was followed, where images with poor exposure, color balance issues, and the presence of a foreign object within the field of view were discarded (Brown et al., 2020a). However, this QC was applied only to the manually collected DHPs. Raw images were processed to obtain the gap fraction and the fraction of intercepted PAR (FIPAR) with HemiPy (Brown et al., 2023). FIPAR is derived as opposed to FAPAR, as plant material is assumed to be completely absorbing, whereas in reality, foliage transmits a small proportion of light in the visible domain. However, previous work has shown differences between FAPAR and FIPAR are typically negligible (Gobron et al., 2006; Li et al., 2021; Wojnowski et al., 2021), so we used the terms interchangeably hereafter. Prior to classification, HemiPy incorporates pre-processing steps (stretching, gamma correction) to enhance the image quality for better image classification between the background

Table 2
Theoretical uncertainties used for estimating FAPAR.

Uncertainty term	Influence	Reference
Calibration (u_{cal})	± 5 %	Apogee Instruments (2020)
Measurement repeatability (u_{rep})	± 0.5 %	
Long-term drift (u_{drift})	± 2 % per year	
Non-linearity (u_{dir})	± 1 % (up to 4000 µmol m^{-2} s^{-1})	
Temperature response (u_{temp})	0.06 ± 0.06 % per °C	
Levelling uncertainty (u_{lev})	± 1 %	(Origo et al., 2017)

and foreground (Díaz, 2023; Macfarlane et al., 2014). Once classified, FAPAR was calculated according to the instantaneous black-sky definition at 10:00 local solar time as

$$FAPAR = 1 - \overline{P(\Theta_{SZA})} \qquad (11)$$

where $\overline{P(\Theta_{SZA})}$ is the mean gap fraction of a zenith ring centred at the solar zenith angle at 10:00 local solar time over all azimuth cells and images analysed. HemiPy also calculates the uncertainty of the FAPAR as the standard error of the mean gap fraction over all azimuth cells and images.

2.5.4. Metrics of comparison

The agreement between 2f- vs. 4f-FAPAR, instantaneous FAPAR vs. daily integrated FAPAR, and DHP-derived FAPAR vs. WSNs FAPAR across sites was evaluated using statistical metrics including the coefficient of determination (R^2), root mean square error (RMSE), normalized root mean square error (NRMSE), bias, and slope. The RMSE represents the square root of the average of the squared difference between two variables, whereas bias measures the average difference between them. A positive bias indicates the overestimation with respect to the reference value, and a negative bias indicates the underestimation. NRMSE is computed by dividing the RMSE by the mean of the reference data. To assess compliance against CEOS requirements, the instantaneous 2f-FAPAR was evaluated by considering the instantaneous 4f-FAPAR as the reference; i.e., the proportion of 2f-FAPAR values falling within both an absolute difference of 0.005 units and a relative difference of 10 % of the reference 4f-FAPAR values was determined.

3. Results

3.1. Implementation of QC

QC was applied to the whole dataset before estimating 2f- and 4f-FAPAR for each study site. These steps are crucial for identifying valid measurements among the continuously recorded datasets. We observed that the number of samples gradually reduced at each step (Table S2.1). Particularly, the implication of energy balance QC is very important; they showed 14.30 % and 10.80 % of data loss in the VAS and LSS sites, respectively. Similarly, another useful and effective QC step, based on the K_t value implementation, identified 18.70 % of the data at the HNP site as cloudy. Restricting the zenith angle to within 80° also had a significant impact in reducing the number of samples, by approximately 10 % at each of our study sites. Lastly, the percentile outliers removed from each 10° zenith angle bin resulted in the identification of approximately 2.7 % of the dataset as outliers. Before applying all the QC steps, we visually inspected the trend and data distribution of each flux and their combination by plotting (Fig. 5) each day's dataset, which has a 5-minute frequency. Here, as an example, we depicted PPFD for daily and individual fluxes, which were the mean of all the nodes at the HNP site. It was noticed that after applying all the QC, the average intensity value of PPFD (Fig. S3.1) changed, which provided more robust results.
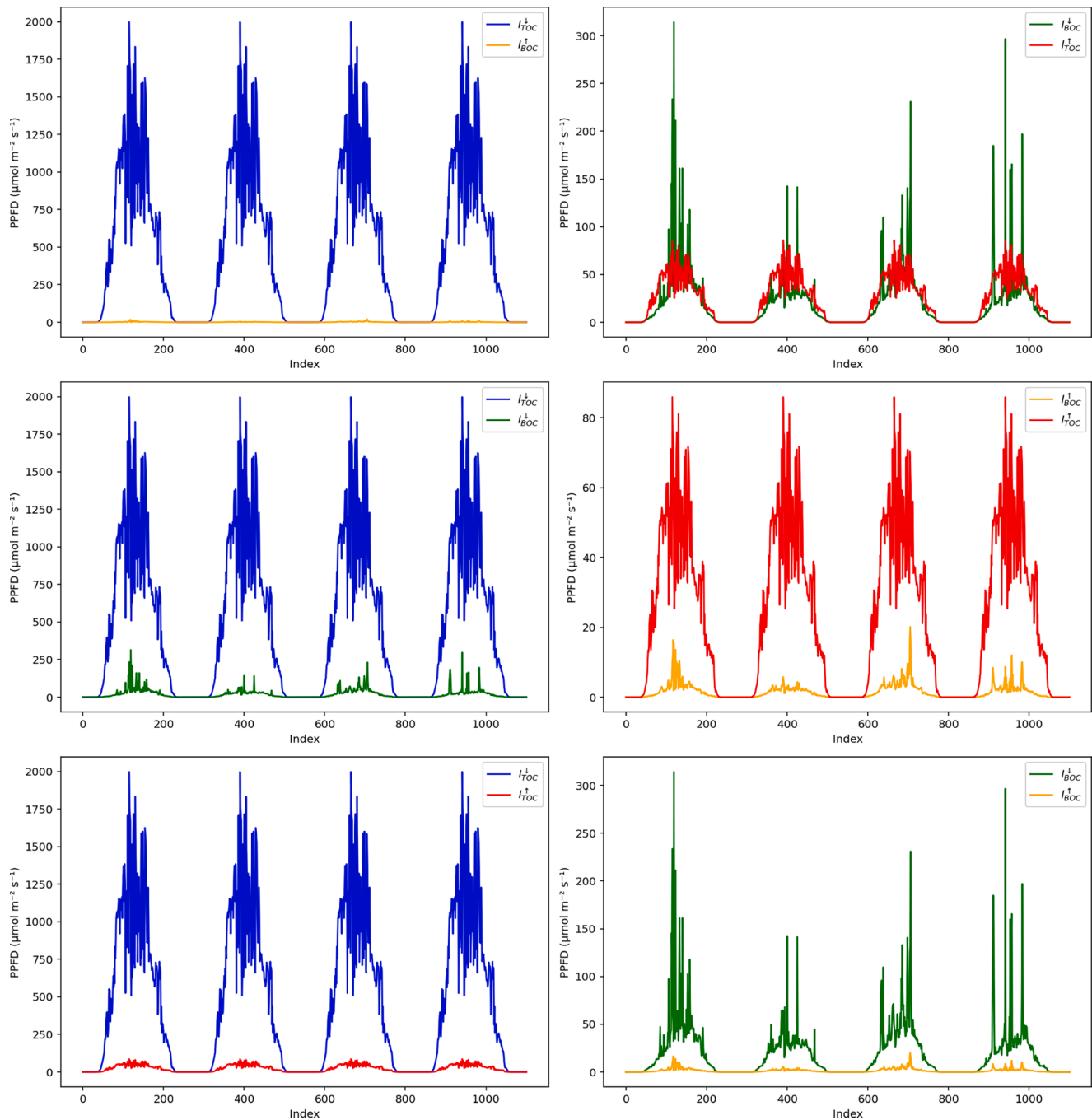
3.2. Comparison between 2f- and 4f-FAPAR

At VAS, 2f-FAPAR and 4f-FAPAR demonstrated strong agreement with R^2 values always greater than 0.99 and low RMSE (0.03) for both instantaneous and daily integrated comparisons (Fig. 6). In terms of systematic differences, a slight positive bias (0.02 for both instantaneous and daily integrated) indicated minor overestimation by 2f-FAPAR. Furthermore, the slopes of >0.96 suggested a slight compression of the measurements' dynamic range, where 2f-FAPAR underestimates the sensitivity of 4f-FAPAR across the full range of values. Mean instantaneous FAPAR values (Table 3) were slightly higher for 2f-FAPAR than 4f-FAPAR, and the mean uncertainties for the ESU were identical for 4f-

Fig. 5. Depicts an example of the pattern and comparison of all the fluxes between each other. This figure was plotted for the date 19th May 2023 for the HNP site. Each sub-plot indicates the combination of any two fluxes among the four fluxes. Two responsible fluxes are coming from the installed TOC tower, and another two fluxes are coming from the BOC installed sensors. Four cycles in each plot represent the four responsible valid nodes for the measurements on that day, which are installed at the BOC.

FAPAR and 2f-FAPAR. Daily aggregation slightly increased the mean values while substantially reducing the mean uncertainties.

Results at HNP also revealed strong agreement between 2f-FAPAR and 4f-FAPAR, with an R^2 value of 0.99 and RMSE of 0.04 for both instantaneous and daily integrated time scales. 2f-FAPAR and 4f-FAPAR had a consistent positive bias (0.04) and slopes >1, indicating minor overestimation across the 2f-FAPAR range (Fig. 6). Mean instantaneous as well as the daily integrated 2f-FAPAR and 4f-FAPAR were both higher (Table 3), with notably low uncertainties. Daily aggregation further stabilized mean daily integrated FAPAR values and reduced the mean uncertainties.

At LSS, the agreement between 2f-FAPAR and 4f-FAPAR remained strong, with R^2 values of 0.99 for both instantaneous and daily integrated time scales. RMSE values were the lowest among all three sites (0.01 for instantaneous daily integrated), and biases were also minimal (0.01 for instantaneous, and daily integrated). The slopes confirm high consistency between 2f- and 4f-FAPAR for both instantaneous as well as the daily integrated FAPAR (Fig. 6).

Time series for each site for both instantaneous and daily integrated 2f- and 4f-FAPAR showed prominent seasonal patterns for the VAS and HNP, but not the LSS site (Fig. 7). Overall, at all sites, instantaneous and daily integrated 2f- and 4f-FAPAR were temporally consistent over a
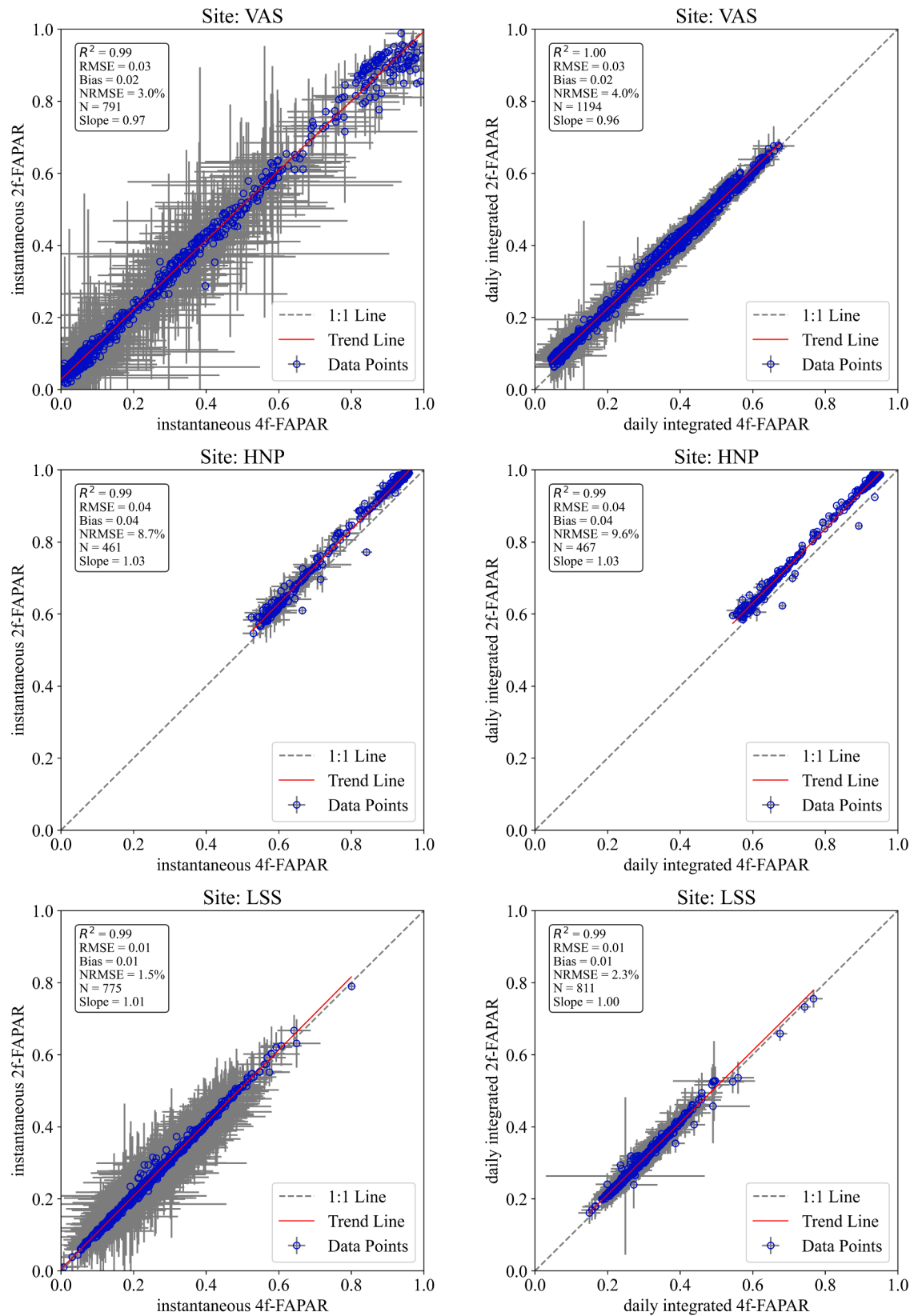
Fig. 6. Visualization of statistical comparison between 2f- and 4f-FAPAR estimation across three sites (VAS, HNP, LSS). Each row of this figure layout represents a different site, whereas each column represents a different timescale (e.g., instantaneous and daily integrated).

Table 3
Site-wise intercomparison of mean FAPAR and mean uncertainty between 2f- and 4f-FAPAR, and percentage of the dataset that meets the GCOS requirements for each site.

Site	VAS		HNP		LSS	
FAPAR	2f-	4f-	2f-	4f-	2f-	4f-
Mean FAPAR (instantaneous)	0.31	0.29	0.85	0.82	0.26	0.24
Mean Uncertainty (instantaneous)	0.07	0.07	0.01	0.01	0.06	0.07
Mean FAPAR (daily integrated)	0.32	0.30	0.86	0.83	0.30	0.29
Mean Uncertainty (daily integrated)	0.03	0.03	0.01	0.01	0.03	0.03
GCOS requirements met	47.14 %		99.78 %		92.00 %	

long period.

3.3. Instantaneous vs. daily integrated FAPAR

Since the 2f-FAPAR and 4f-FAPAR estimates were highly consistent, the comparison between instantaneous and daily integrated FAPAR was restricted to 2f-FAPAR for simplicity. At VAS, the mean instantaneous 2f-FAPAR was 0.31, with an uncertainty of 0.07. Daily aggregation resulted in a higher mean 2f-FAPAR with reduced uncertainty, demonstrating the stabilizing effect of temporal averaging. Variability was moderate, with standard deviations of 0.28 for instantaneous and 0.18 for daily integrated 2f-FAPAR. Agreement statistics (Table 4) between instantaneous and daily integrated 2f-FAPAR revealed a moderately strong correlation ($R^2 = 0.67$) with a moderate RMSE of 0.17 (Fig. 8). The bias and slope suggest that daily integrated FAPAR tended to be slightly higher than instantaneous FAPAR on average.

At HNP, the mean instantaneous 2f-FAPAR was high, but daily aggregation marginally increased the mean FAPAR and reduced the mean uncertainty. Variability in instantaneous (standard deviation = 0.15) and daily integrated (standard deviation = 0.14) 2f-FAPAR was almost similar. Agreement statistics showed the highest R^2 (= 0.97) and the lowest RMSE (= 0.03) among the three sites (Table 4), demonstrating excellent alignment between instantaneous and daily integrated measurements with a minimal bias (Fig. 8). Their slope indicates a high degree of consistency, though instantaneous FAPAR values tend to be slightly lower.

LSS exhibited the lower mean 2f-FAPAR values for both instantaneous and daily integrated 2f-FAPAR, and the mean uncertainty was also lower. Agreement statistics revealed the lowest R^2 (= 0.34), indicating a weaker correlation (Table 4) between instantaneous and daily integrated 2f-FAPAR. The RMSE and NRMSE were comparable to VAS, reflecting greater variability (Fig. 8). The standard deviation was higher for instantaneous 2f-FAPAR (= 0.12) compared to daily integrated 2f-FAPAR (= 0.06). The bias and slope suggest that daily integrated 2f-FAPAR is consistently higher than instantaneous values.

The time series plots (Fig. 8) of instantaneous and daily integrated 2f-FAPAR for the VAS site consistently showed a strong alignment, though some deviation and variability were observed, especially at the transitional season. The temporal pattern of HNP proves that the canopy cover is very dense, and both instantaneous and daily integrated 2f-FAPAR exhibited strong clustering with minimal variability. In contrast, the LSS site showed stronger variability across the entire time period, but a clear seasonal peak was absent, and the agreement between instantaneous and daily integrated 2f-FAPAR was very weak.

3.4. Comparison of WSNs and DHP estimated FAPAR

The comparison between the WSNs-derived 2f-FAPAR and DHP-derived FAPAR reveals distinct patterns for both instantaneous and daily timescales at VAS and HNP. For instantaneous 2f-FAPAR versus DHP-derived instantaneous FAPAR, VAS showed moderate agreement with an R^2 of 0.39, an RMSE of 0.34, and a positive bias of 0.23 (Fig. 9),

indicating a notable overestimation of 2f-FAPAR. The slope of 0.22 further confirms a weak linear relationship, with the trend line deviating substantially from the ideal 1:1 line. The daily integrated 2f-FAPAR improved the agreement with an R^2 of 0.56, RMSE of 0.15, and bias reduced to 0.12. The NRMSE decreased to 35.06 %, and the slope improved to 0.62, indicating a comparatively stronger linear trend than the instantaneous data, but still shows considerable deviation.

In contrast, at HNP, the agreement between 2f-FAPAR and DHP-derived instantaneous FAPAR was better than VAS, with an R^2 of 0.76 and a comparatively lower RMSE of 0.14. The positive lower bias (= 0.12) indicates consistent overestimates of the instantaneous 2f-FAPAR. The slope of 1.04 suggests that while the model is generally overestimating FAPAR, this overestimation becomes more pronounced as the FAPAR values get higher. However, the daily integrated 2f-FAPAR comparison exhibited almost identical agreement to instantaneous 2f-FAPAR, with an R^2 of 0.74 in HNP. The RMSE and bias were similar (Fig. 10), while the slope increased further to 1.14, highlighting a consistent overestimation of daily integrated 2f-FAPAR as the FAPAR value increases.

4. Discussion

4.1. Consistency of 2f- and 4f-FAPAR estimates

The findings demonstrated strong consistency between 2f-FAPAR and 4f-FAPAR estimates across all three study sites, with higher correlation coefficients ($R^2 \geq 0.99$) and other low error metrics such as RMSE, bias, and NRMSE for both instanteneous and daily integrated timescales. A minor positive bias (0.01 to 0.04) indicates that 2f-FAPAR slightly overstimates 4f-FAPAR, though the magnitude of this bias is minimal, reinforcing the reliability of 2f-FAPAR as an efficient alternative to 4f-FAPAR. These results highlight the 2f-FAPAR system's practicality, as it reduces measurement complexity, and operational costs, making it suitable for large-scale and real-time applications (Widlowski, 2010).

Theoretically, the 2f-FAPAR estimate should be higher than the 4f-FAPAR due to its omission of the upwelling fluxes, which are captured by 4f-FAPAR, and this was observed in all of our study sites. At our vineyard site (VAS), it was observed that in the summer, specifically in July and August, sometimes 4f-FAPAR was higher than 2f-FAPAR, which suggests a high sensitivity to specific illumination and bare soil reflectivity in fragmented row crop arrangements. While the HNP exhibited a highly consistent higher 2f-FAPAR, a few days in January and February were observed with an opposite trend, and background snow albedo could be a possible reason. HNP deciduous forest is recognized for its dense canopy, factors such as unmanaged dead wood and limited undergrowth lead to a significant accumulation of dead leaves on the forest floor, and the presence of natural gaps due to wind throw and tree mortality (Thiel et al., 2020) could increase ground reflectivity. Similarly, we observed that a few 4f-FAPAR measurements were consistently higher than 2f-FAPAR in an open savanna site (LSS) during the spring and early summer. The discontinuous open canopy structure (Feltrin et al., 2016; Finch et al., 2004), with grass understory and sandy loam soil formed over weathered sandstone (Loewensteiner et al., 2021), could create a highly reflective surface. However, the observed agreement between methods from our study suggests that for most ecological and remote sensing applications, 2f-FAPAR could be acceptable over 4f-FAPAR as it has the potential to provide sufficient accuracy. The spatial complexity and canopy height may impact the reliable sampling of radiation fluxes, which are stronger in forest ecosystems than in agriculture or young tree plantations (Widlowski, 2010). Our tall, dense HNP site likely results in a larger measurement footprint as the PAR sensors are at 8 m above the canopy, and it is integrating upwelling radiation over a wider area, averaging out localized variations. Conversely, LSS and VAS had a comparatively smaller measurement footprint due to a comparatively lower canopy height, leading to more sensitivity to local variation.
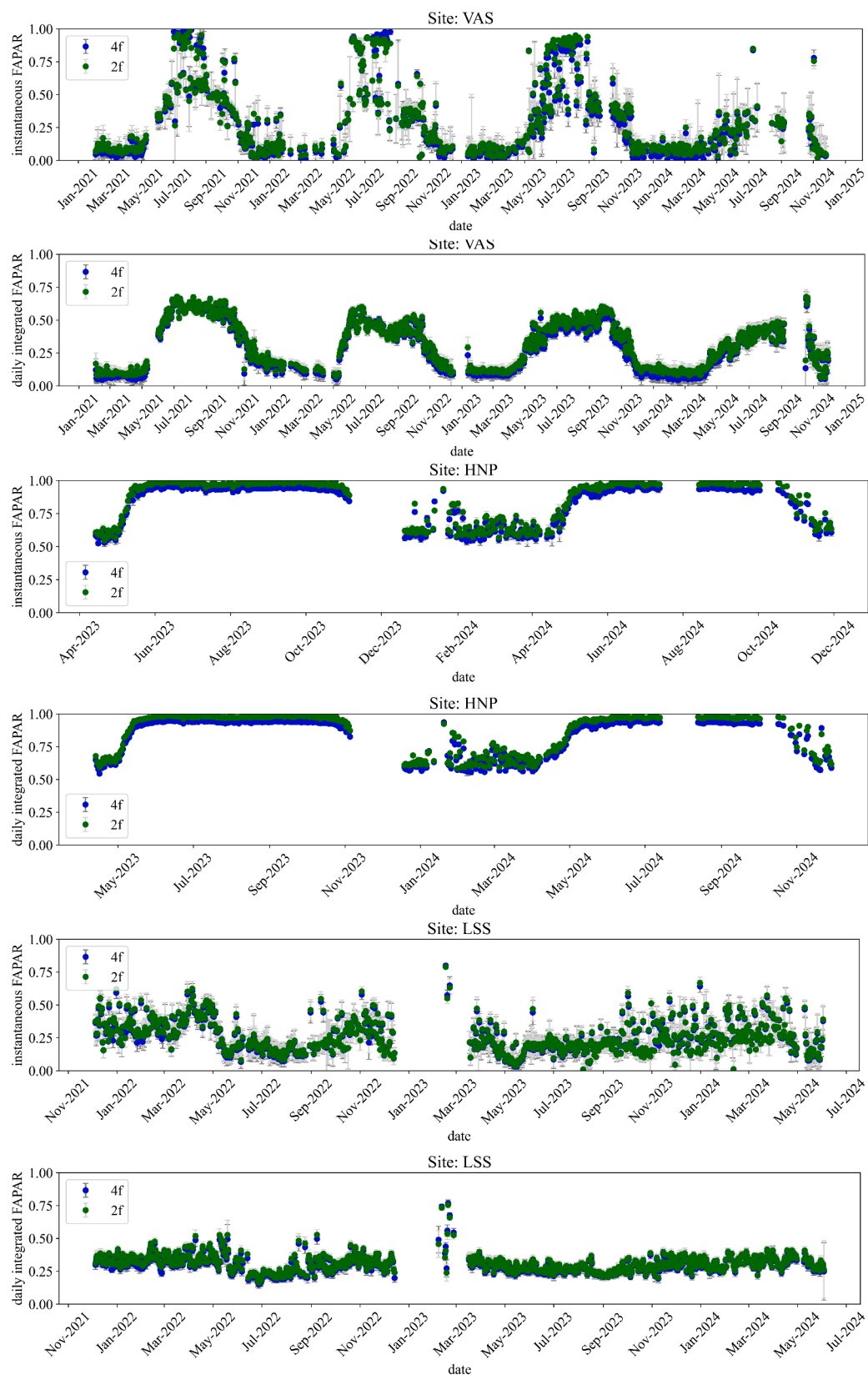
Fig. 7. Comparison of 2f- and 4f-FAPAR time series across three sites (VAS, HNP and LSS). Each site has two plots, one for instantaneous FAPAR and just below another one for daily integrated FAPAR.

Table 4

Statistical intercomparison and agreement between instantaneous and daily integrated 2f-FAPAR for each site.

Statistical Metrics	VAS	HNP	LSS
Instantaneous			
Mean 2f-FAPAR	0.31	0.85	0.26
Mean Uncertainty	0.07	0.01	0.06
Daily Integrated			
Mean 2f-FAPAR	0.32	0.86	0.30
Mean Uncertainty	0.03	0.01	0.03
Instantaneous vs Daily Integrated			
R^2	0.67	0.97	0.34
RMSE	0.17	0.03	0.11
Bias	−0.01	0.01	0.05
NRMSE	17.5 %	6.20 %	13.80 %
Slope	0.51	0.91	0.28

Time series at the three different sites demonstrated the consistency between 2f and 4f-FAPAR. At VAS, FAPAR prominently followed the seasonality of the vineyard. In the summer, the grapevine canopy achieves its density, resulting in high FAPAR; winter leads to lower FAPAR; and in spring, the FAPAR gradually increases during the post-bud break period of the vine. Time series of FAPAR at HNP suggests the site has a dense canopy with high and relatively consistent radiation absorption throughout the year. The lower FAPAR values in April-May correspond to the leaf development stages, with both years following similar patterns. Time series of FAPAR at LSS indicate that the savanna woodland has sparse and dynamic canopy cover, but without prominent seasonality. Sometimes, a potential peak was observed around August-September.

The choice between 2f-FAPAR and 4f-FAPAR depends on the application's requirements. On the basis of previous studies, it is expected that the additional fluxes reduce bias and improve the FAPAR estimates
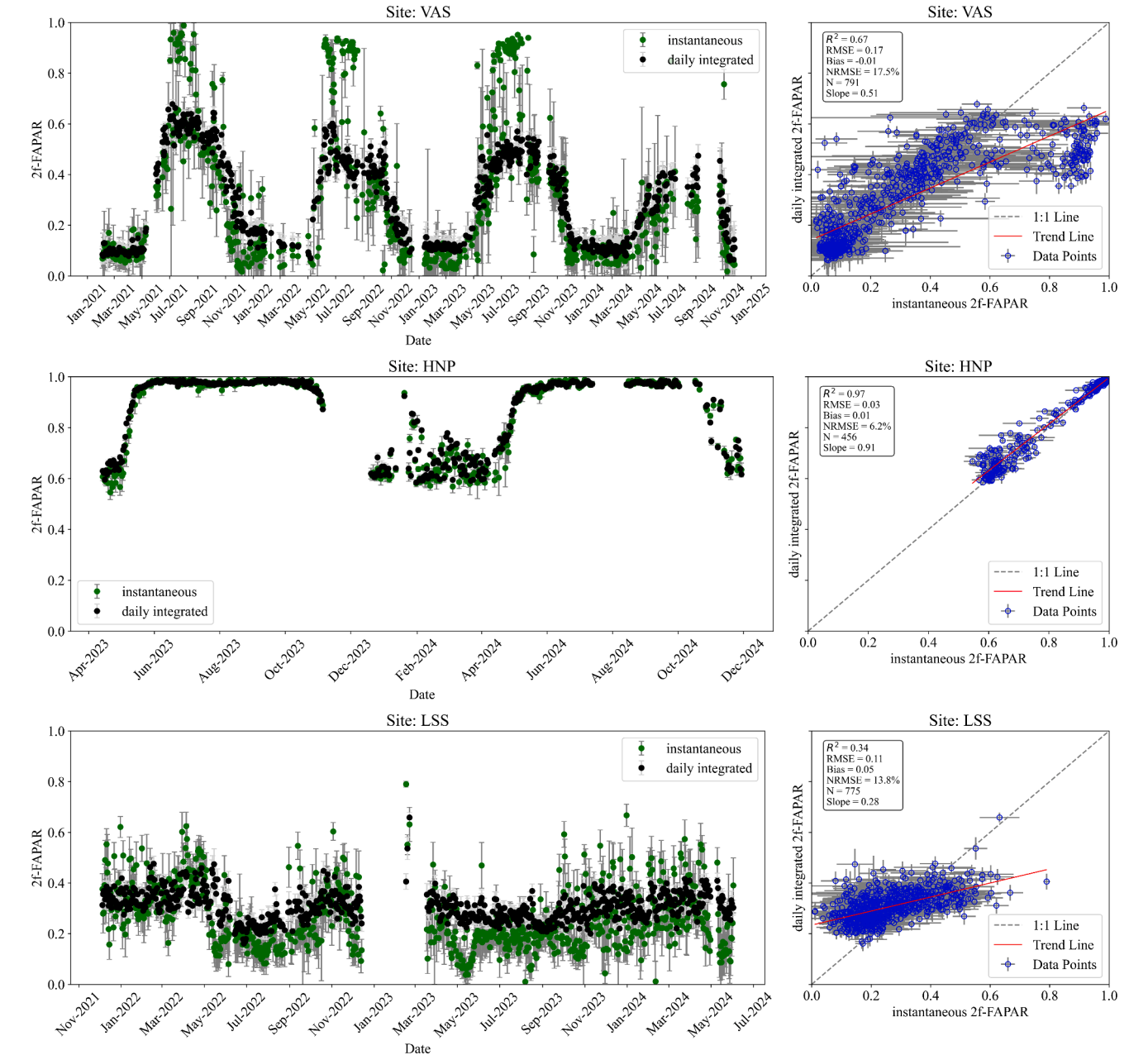
Fig. 8. Temporal variation and corresponding statistical comparison between instantaneous and daily integrated 2f-FAPAR across three sites. Each row in the figure layout represents the individual sites.
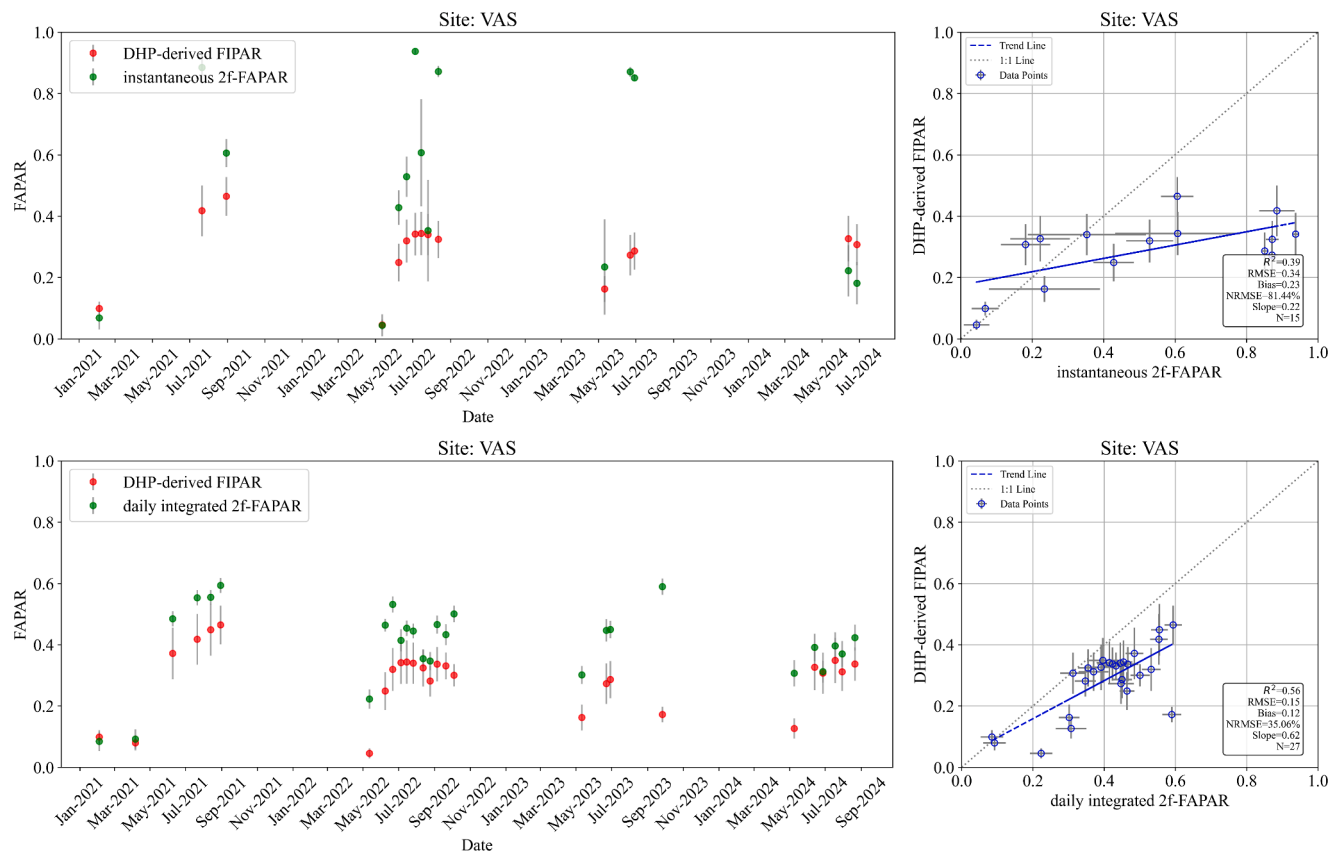
Fig. 9. Intercomparison between WSNs-derived FAPAR vs DHP-based FAPAR for the site VAS. The first row is for instantaneous 2f-FAPAR, and the second row represents the daily integrated 2f-FAPAR.

(Putzenlechner et al., 2020), but our results demonstrated minimal bias between 2f- and 4f-FAPAR measurements. Overall, the study underscores the robustness of 2f-FAPAR as a reliable tool for FAPAR estimation.

4.2. Consistency between instantaneous and daily integrated FAPAR

The analysis of instantaneous versus daily integrated 2f-FAPAR measurements across VAS, HNP, and LSS underscores the importance of measuring FAPAR at both timescales to meet different research and operational objectives. Instantaneous FAPAR measurements, which are captured around a given local solar time to align with typical satellite overpasses, are essential for validating the satellite land products (Zhang et al., 2023). Similarly to other studies (Chen et al., 2020), in our future work, we will validate the Sentinel-3 FAPAR products with our in-situ FAPAR measurement, which motivates us to choose the instantaneous time window to match with satellite overpass time. These measurements provide high temporal resolution data that reflect the immediate impact of solar radiation on light absorption by the vegetation canopy, enabling detailed insights into diurnal variations and short-term photosynthetic dynamics. Conversely, daily integrated FAPAR measurements offer a smoothed representation of vegetation light absorption by averaging out transient fluctuations caused by weather and diurnal cycles. This makes them particularly valuable for long-term ecological monitoring, agricultural modeling, and climate studies, where consistent and reliable trends are more informative than momentary snapshots.

Comparison between the two timescales reveals that daily integrated FAPAR generally exhibits lower uncertainties and reduced variability across all three sites. For instance, at VAS and HNP, daily integrated measurements not only reduced uncertainty but also maintained strong agreement with instantaneous FAPAR values (0.67 and 0.97, respectively). These findings suggest that daily integration provides a more

reliable and stable estimate of vegetation light absorption, particularly in dense cover environments like HNP. HNP showed a consistently higher FAPAR value, which may be an overestimation, though research has found higher FAPAR values in deciduous forests (Zheng et al., 2022). In contrast, the agreement between the two timescales was weaker at LSS, where the vegetation is more heterogeneous ($R^2 = 0.34$, RMSE = 0.11) due to the sparse open vegetation ecosystem, although daily integrated measurements still demonstrated reduced uncertainty and variability. These results emphasize the need to consider site-specific characteristics when interpreting and applying FAPAR measurements. This study shows that the instantaneous FAPAR is lower than the daily integrated FAPAR, which is similar to other studies in forest and broadleaf crop sites (Chen et al., 2020; Zhang et al., 2021). Research also suggests that at very high vegetation density, FAPAR saturates, and if the FAPAR becomes greater than 0.8, the difference between these two FAPAR estimates reduces (Zhang et al., 2021; Zhao et al., 2018), which is reflective of our HNP site. Many studies (Chen et al., 2020; Majasalmi et al., 2017; Zhang et al., 2023) attempted to establish the relationship between these two time frames of FAPAR values; some approximated that instantaneous FAPAR values are the same as daily integrated FAPAR values (Camacho et al., 2013; Ma et al., 2022). However, few studies reported their apparent differences in terms of overestimation and underestimation, which suggests that they vary based on the vegetation growth stages and topographical location (Senna et al., 2005; Zhang et al., 2021). Very dense forest structure causes the saturation, which might cause the high 2f-FAPAR in HNP, as minimal light penetrates toward the ground. However, it would also be worthwhile to check the sensor calibration, position, and any potential obstruction for the $I_{BOC}^{\downarrow}$.
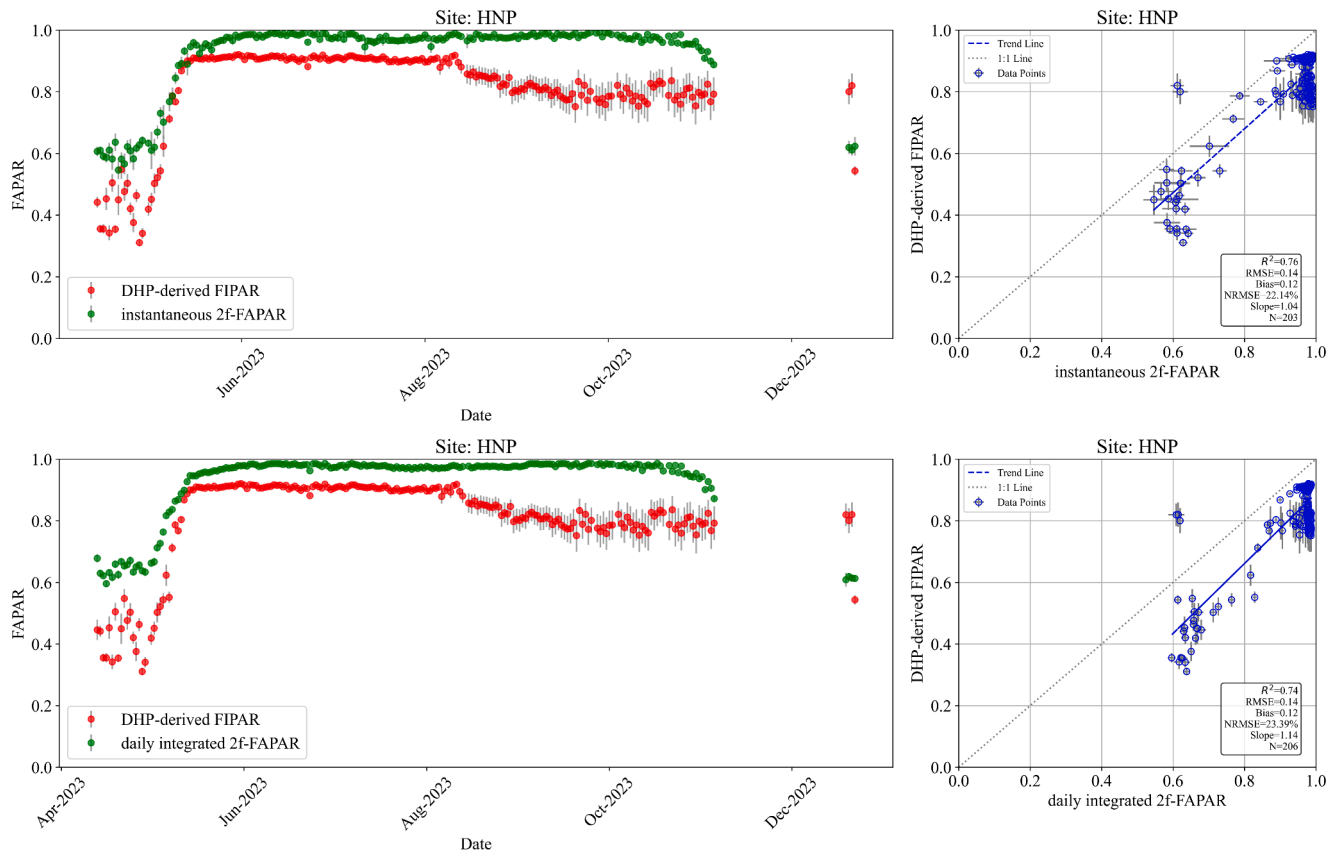
Fig. 10. Intercomparison between WSNs-derived FAPAR vs DHP-based FAPAR for the site HNP. The first row is for instantaneous 2f-FAPAR, and the second row represents the daily integrated 2f-FAPAR.

4.3. Intercomparison between WSNs- FAPAR and DHP-based FAPAR

The comparison between WSNs-derived 2f-FAPAR and DHP-derived FAPAR underscores the strengths and limitations of these methods in capturing vegetation light absorption. At VAS, both instantaneous and daily 2f-FAPAR showed moderate agreement with DHP-derived FAPAR, as indicated by R^2 values (0.39 and 0.56, respectively) with an RMSE of 0.34 to 0.15. Due to the limited number of samples in VAS, it is difficult to make firm conclusions regarding statistical consistency. In HNP, the results highlight a more pronounced agreement between instantaneous and daily integrated 2f-FAPAR comparison with DHP-derived FAPAR. They closely followed the temporal pattern with a minimal over-estimation of 2f-FAPAR, exhibiting a bias of 0.12 for instantaneous and daily integrated 2f-FAPAR.

Theoretically, DHP-derived FAPAR should be typically higher than the actual 2f-FAPAR, assuming the complete absorption of intercepted light, and DHP primarily estimates the FAPAR based on the gap fraction of the canopy. Additionally, DHP doesn't explicitly differentiate between interception by green and non-green elements of the plants, as DHP works based on the principle of gap fraction. In our study sites, the biases may arise from the structural complexity of the canopy at HNP and in VAS, which affects the light transmission captured by the DHP (Li et al., 2021). Due to the dense, multi-layered canopy system in HNP, multiple scattering and absorption events may not be accurately captured by DHP, which may result in a lower DHP-based FAPAR compared to the 2f-FAPAR measuring system. Research also found that FAPAR was underestimated in dense canopies where the plant area index (PAI) is higher (Brown et al., 2020a). The bias of the 2f-FAPAR may arise due to the positions of the sensors, whereas in a field campaign, the biases are averaged out. So, in a heterogeneous ecosystem, identifying the best sensor locations is important. Understanding the phenology of the understorey vegetation is also important;

however, their growth is not homogeneous over the study area, which may create an extra logistical difficulty. The installed towers in the forests are prone to environmental dust and bird droppings, which may impact results, so repeated cleaning and calibration are essential. These factors all could cause higher 2f-FAPAR, and further investigation into them is required. The choice of FAPAR estimation method and timescale should consider the specific ecological context and research goals. Manual DHP systems through field campaigns could provide valuable spatially explicit canopy structural information, but may be limited in capturing temporal dynamics. Though automated DHP systems were installed in our HNP site, providing temporal continuity, these auto-mated DHP systems are fixed with automatic camera settings for image capture. In natural environments, substantial variations in illumination could be observed due to changes in sunlight and cloud cover.

4.4. Limitations and future directions

Overall, in our study, we observed the positive significance and implications of the FAPAR estimation framework for different vegetation types. Though the limitations of our study could be that we didn't consider the understorey vegetation for our analysis. A DHP-based study showed that neglecting the understory layer leads to a systematic underestimation of FAPAR, with an average error of 0.07 to 0.61 (Brown et al., 2020a). Yan et al. (2016) also suspected an overestimation in their study due to the lack of understorey in-situ measurements. However, multiple studies (Putzenlechner et al., 2020, 2019a; Sanchez-Azofeifa et al., 2022) have been found where understorey FAPAR measurements were not included in their wireless sensor network-based approach. Theoretically, understorey vegetation would have an impact on the total overall FAPAR estimation for the ecosystem, but it doesn't change dynamically (Liu et al., 2024). In our future study, these understorey measurements would be included. Our DHP-based analysis could be

subject to a lack of statistical uniformity due to variation in sampling across sites. The VAS site was limited by a small sample size from manual campaigns, while the HNP site provided robust, confident results based on a substantial sample size of 161, due to automated DHP observations. Furthermore, DHP data from the LSS site were not included in this analysis, which may impact the overall representativeness of our findings. Another limitation of our current study could be identifying the threshold between cloud and clear sky using the K_t value and its distribution. Future work could explore the use of advanced sensor networks or instruments (e.g., Delta-T BF5, the Baseline Surface Radiation Network (BSRN), a radiometer with a shadowband) to measure the diffuse sky solar irradiance (Ameen et al., 2018; Foyo-Moreno et al., 2018; Lozano et al., 2023b). Those measurements would be useful to understand the impact of clouds on FAPAR estimation and evaluate the accuracy of the threshold.

5. Conclusions

This study provides comprehensive insights into the reliability and applicability of 2f-FAPAR measurements across different temporal scales and different vegetation types, and their comparison with 4f-FAPAR and DHP-derived FAPAR. First, we observed a strong agreement between 2f- and 4f-FAPAR across all sites, indicating that 2f measurements can serve as a reliable alternative to the more complex and cost-intensive 4f setup. While 2f-FAPAR exhibited slight overestimation, the discrepancies were minimal and did not compromise the accuracy substantially. Second, daily integrated 2f-FAPAR demonstrated greater stability and lower uncertainty compared to instantaneous measurements. This highlights the importance of daily integrated FAPAR for ecosystem modeling and understanding canopy-level light dynamics. Nevertheless, instantaneous FAPAR remains essential for satellite product validation, as it better corresponds to the temporal properties of satellite overpasses. Third, 2f-FAPAR showed good agreement with DHP-derived FAPAR, emphasizing its reliability. Given that DHP measurements are typically manual and can be prone to increased uncertainty due to human error, the 2f WSNs of the PAR system emerge as a robust and automated alternative. The 2f system not only reduces human intervention but also provides continuous measurements that are essential for long-term ecosystem monitoring and modeling. In conclusion, this research underscores the efficacy of 2f-FAPAR as a cost-effective, reliable, and automated tool for canopy light absorption studies. It offers substantial advantages in reducing measurement complexity while ensuring robust data quality, making it a promising alternative to traditional methods in both ecological research and remote sensing validation.

CRediT authorship contribution statement

Somnath Paramanik: Writing – original draft, Software, Methodology, Investigation, Formal analysis, Data curation, Conceptualization. **Harry Morris:** Writing – review & editing, Methodology, Investigation, Conceptualization. **Rémi Grousset:** Methodology, Data curation. **Gabriele Bai:** Writing – review & editing, Visualization. **Christophe Lerebourg:** Writing – review & editing, Visualization, Resources, Data curation. **Ernesto Lopez-Baeza:** Writing – review & editing, Visualization, Resources. **Ana Pérez-Hoyos:** Writing – review & editing, Visualization. **David Garcia-Rodriguez:** Writing – review & editing, Visualization, Investigation. **Darius Culvenor:** Writing – review & editing, Visualization, Validation, Investigation. **Alexander Knohl:** Writing – review & editing, Visualization, Resources, Investigation. **Anne Klosterhalfen:** Writing – review & editing, Validation, Resources, Investigation. **Frank Tiedemann:** Writing – review & editing, Visualization. **Christian Lanconelli:** Writing – review & editing, Visualization, Investigation. **Marco Clerici:** Writing – review & editing, Visualization, Investigation. **Nadine Gobron:** Writing – review & editing, Visualization, Investigation. **Luke A. Brown:** Writing – review & editing, Visualization, Validation, Methodology, Investigation, Conceptualization. **Finn James:** Software, Data curation. **Stefan Maier:** Writing – review & editing, Visualization, Resources. **Fabrizio Niro:** Visualization, Validation, Investigation. **Jadunandan Dash:** Writing – review & editing, Visualization, Validation, Supervision, Methodology, Investigation, Conceptualization.

Declaration of competing interest

The authors declare that they have no known competing financial interests or personal relationships that could have appeared to influence the work reported in this paper.

Supplementary materials

Supplementary material associated with this article can be found, in the online version, at doi:10.1016/j.agrformet.2025.110904.

Data availability

Data will be made available on request.

References

Apogee Instruments, 2020. Retrieved from. https://www.apogeeinstruments.com/content/SQ-100-200-300-spec-sheet.pdf.

Ameen, B., Balzter, H., Jarvis, C., 2018. Quality control of global horizontal irradiance estimates through bsrn, toacs and air temperature/sunshine duration test procedures. Climate 6, 69.

Bai, G., Lerebourg, C., Brown, L., Morris, H., Dash, J., Clerici, M., Gobron, N., 2022. GBOV (Ground-Based Observation for Validation): a copernicus service for validation of land products. In: IGARSS 2022-2022 IEEE International Geoscience and Remote Sensing Symposium. IEEE, pp. 4304–4307.

Baret, F., Andrieu, B., Steven, M., 1993. Gap frequency and canopy architecture of sugar beet and wheat crops. Agric. For. Meteorol. 65, 261–279.

Brown, L.A., Camacho, F., García-Santos, V., Origo, N., Fuster, B., Morris, H., Pastor-Guzman, J., Sánchez-Zapero, J., Morrone, R., Ryder, J., 2021a. Fiducial reference measurements for vegetation bio-geophysical variables: an end-to-end uncertainty evaluation framework. Remote Sens. 13, 3194.

Brown, L.A., Dash, J., Lidón, A.L., Lopez-Baeza, E., Dransfeld, S., 2019. Synergetic exploitation of the Sentinel-2 missions for validating the Sentinel-3 ocean and land color instrument terrestrial chlorophyll index over a vineyard dominated mediterranean environment. IEEE J. Sel. Top. Appl. Earth Obs. Remote Sens. 12, 2244–2251.

Brown, L.A., Fernandes, R., Djamai, N., Meier, C., Gobron, N., Morris, H., Canisius, F., Bai, G., Lerebourg, C., Lanconelli, C., 2021b. Validation of baseline and modified Sentinel-2 Level 2 Prototype Processor leaf area index retrievals over the United States. ISPRS J. Photogramm. Remote Sens. 175, 71–87.

Brown, L.A., Meier, C., Morris, H., Pastor-Guzman, J., Bai, G., Lerebourg, C., Gobron, N., Lanconelli, C., Clerici, M., Dash, J., 2020a. Evaluation of global leaf area index and fraction of absorbed photosynthetically active radiation products over North

America using copernicus ground based observations for validation data. Remote Sens. Environ. 247, 111935.

Brown, L.A., Morris, H., Albero, E., Lopez-Baeza, E., Tiedemann, F., Siebicke, L., Knohl, A., da Silva Gomes, C., Bai, G., Lerebourg, C., 2021c. Potential of automated digital hemispherical photography and wireless quantum sensors for routine canopy monitoring and satellite product validation. In: 2021 IEEE International Geoscience and Remote Sensing Symposium IGARSS. IEEE, pp. 53–56.

Brown, L.A., Morris, H., Leblanc, S., Bai, G., Lanconelli, C., Gobron, N., Meier, C., Dash, J., 2023. HemiPy: a Python module for automated estimation of forest biophysical variables and uncertainties from digital hemispherical photographs. Methods Ecol. Evol. 14, 2329–2340.

Brown, L.A., Ogutu, B.O., Dash, J., 2020b. Tracking forest biophysical properties with automated digital repeat photography: a fisheye perspective using digital hemispherical photography from below the canopy. Agric. For. Meteorol. 287, 107944.

Camacho, F., Cernicharo, J., Lacaze, R., Baret, F., Weiss, M., 2013. GEOV1: LAI, FAPAR essential climate variables and FCOVER global time series capitalizing over existing products. Part 2: validation and intercomparison with reference products. Remote Sens. Environ. 137, 310–329.

Camacho, F., Martínez-Sánchez, E., Brown, L.A., Morris, H., Morrone, R., Williams, O., Dash, J., Origo, N., Sánchez-Zapero, J., Boccia, V., 2024. Validation and conformity testing of sentinel-3 green instantaneous FAPAR and canopy chlorophyll content products. Remote Sens. 16.

Cammalleri, C., McCormick, N., Toreti, A., 2022. Analysis of the relationship between yield in cereals and remotely sensed fAPAR in the framework of monitoring drought impacts in Europe. Nat. Hazards Earth Syst. Sci. 22, 3737–3750.

Carbó, E., Juan, P., Anó, C., Chaudhuri, S., Diaz-Avalos, C., López-Baeza, E., 2021. Modeling influence of Soil properties in different gradients of Soil moisture: the case of the Valencia anchor station validation site, Spain. Remote Sens. 13, 5155.

Chen, S., Liu, L., He, X., Liu, Z., Peng, D., 2020. Upscaling from instantaneous to daily fraction of absorbed photosynthetically active radiation (FAPAR) for satellite products. Remote Sens. 12, 2083.

Cleverly, J., Eamus, D., Edwards, W., Grant, M., Grundy, M.J., Held, A., Karan, M., Lowe, A.J., Prober, S.M., Sparrow, B., 2019. TERN, Australia's land observatory: addressing the global challenge of forecasting ecosystem responses to climate variability and change. Environ. Res. Lett. 14, 095004.

D'hont, B., Calders, K., Bartholomeus, H., Whiteside, T., Bartolo, R., Levick, S., Krishna Moorthy, S.M., Terryn, L., Verbeeck, H., 2021. Characterising termite mounds in a tropical savanna with UAV laser scanning. Remote Sens. 13, 476.

Díaz, G.M., 2023. Optimizing forest canopy structure retrieval from smartphone-based hemispherical photography. Methods Ecol. Evol. 14, 875–884.

D'Odorico, P., Gonsamo, A., Pinty, B., Gobron, N., Coops, N., Mendez, E., Schaepman, M. E., 2014. Intercomparison of fraction of absorbed photosynthetically active radiation products derived from satellite data over Europe. Remote Sens. Environ. 142, 141–154.

Duchon, C.E., O'Malley, M.S., 1999. Estimating cloud type from pyranometer observations. J. Appl. Meteorol. 38, 132–141.

Duffie, J.A., Beckman, W.A., 2013. Solar Engineering of Thermal Processes. John Wiley & Sons.

Feltrin, R.P., Will, R.E., Meek, C.R., Masters, R.E., Waymire, J., Wilson, D.S., 2016. Relationship between photosynthetically active radiation and understory productivity across a forest-savanna continuum. For. Ecol. Manag. 374, 51–60.

Fensholt, R., Sandholt, I., Rasmussen, M.S., 2004. Evaluation of MODIS LAI, fAPAR and the relation between fAPAR and NDVI in a semi-arid environment using in situ measurements. Remote Sens. Environ. 91, 490–507.

Fernandes, R., Brown, L., Canisius, F., Dash, J., He, L., Hong, G., Huang, L., Le, N.Q., MacDougall, C., Meier, C., 2023. Validation of simplified level 2 prototype processor sentinel-2 fraction of canopy cover, fraction of absorbed photosynthetically active radiation and leaf area index products over North American forests. Remote Sens. Environ. 293, 113600.

Finch, D., Bailey, W., McArthur, L., Nasitwitwi, M., 2004. Photosynthetically active radiation regimes in a southern African savanna environment. Agric. For. Meteorol. 122, 229–238.

Foyo-Moreno, I., Alados, I., Alados-Arboledas, L., 2018. A new empirical model to estimate hourly diffuse photosynthetic photon flux density. Atmospheric Res 203, 189–196.

Gielen, B., Acosta, M., Altimir, N., Buchmann, N., Cescatti, A., Ceschia, E., Fleck, S., Hortnagal, L., Klumpp, K., Kolari, P., Lohile, A., Loustau, D., Maranon-Jimenez, S., Manisp, L., Matteucci, G., Merbold, L., Metzger, C., Moureaux, C., Montagnani, L., Nilsson, M., Osborne, B., Papale, D., Pavelka, M., Saunders, M., Simioni, G., Soudani, K., Sonnentag, O., Tallec, T., Tuittila, E., Peichl, M., Pokorny, R., Vincke, C., Wohljahrt, G., 2018. Ancillary vegetation measurements at ICOS ecosystem stations. Int. Agrophysics 32, 20. https://doi.org/10.1515/intag-2017-0048.

Gobron, N., Morgan, O., Adams, J., Brown, L.A., Cappucci, F., Dash, J., Lanconelli, C., Marioni, M., Robustelli, M., 2022. Evaluation of Sentinel-3A and Sentinel-3B ocean land colour instrument green instantaneous fraction of absorbed photosynthetically active radiation. Remote Sens. Environ. 270, 112850.

Gobron, N., Pinty, B., Aussedat, O., Chen, J.M., Cohen, W.B., Fensholt, R., Gond, V., Huemmrich, K.F., Lavergne, T., Mélin, F., 2006. Evaluation of fraction of absorbed photosynthetically active radiation products for different canopy radiation transfer regimes: methodology and results using Joint Research Center products derived from SeaWiFS against ground-based estimations. J. Geophys. Res. Atmospheres 111.

Gobron, N., Pinty, B., Aussedat, O., Taberner, M., Faber, O., Mélin, F., Lavergne, T., Robustelli, M., Snoeij, P., 2008. Uncertainty estimates for the FAPAR operational products derived from MERIS—Impact of top-of-atmosphere radiance uncertainties and validation with field data. Remote Sens. Environ. 112, 1871–1883.

Gobron, N., Pinty, B., Mélin, F., Taberner, M., Verstraete, M.M., Robustelli, M., Widlowski, J.-L., 2007. Evaluation of the MERIS/ENVISAT FAPAR product. Adv. Space Res. 39, 105–115.

Gower, S.T., Kucharik, C.J., Norman, J.M., 1999. Direct and indirect estimation of leaf area index, f(APAR), and net primary production of terrestrial ecosystems. Remote Sens. Environ. 70, 29–51. https://doi.org/10.1016/S0034-4257(99)00056-5.

Gueymard, C.A., 2018. Revised composite extraterrestrial spectrum based on recent solar irradiance observations. Sol. Energy 169, 434–440.

Harris, P., Østergaard, P.F., Tabandeh, S., Söderblom, H., Kok, G., van Dijk, M., Luo, Y., Pearce, J., Tucker, D., Vedurmudi, A.P., 2025. Measurement Uncertainty Evaluation for Sensor Network Metrology. Metrology 5, 3.

Heidenreich, M.G., Seidel, D., 2022. Assessing forest vitality and forest structure using 3D data: a case study from the Hainich National Park, Germany. Front. For. Glob. Change 5, 929106.

Iqbal, M., 1983. Chapter 1 - SUN–EARTH ASTRONOMICAL RELATIONSHIPS. In: Iqbal, M. (Ed.), An Introduction to Solar Radiation. Academic Press, pp. 1–28. https://doi.org/10.1016/B978-0-12-373750-2.50006-9.

Karan, M., Liddell, M., Prober, S.M., Arndt, S., Beringer, J., Boer, M., Cleverly, J., Eamus, D., Grace, P., Van Gorsel, E., 2016. The Australian SuperSite Network: a continental, long-term terrestrial ecosystem observatory. Sci. Total Environ. 568, 1263–1274.

Kloos, S., Klosterhalfen, A., Knohl, A., Menzel, A., 2024. Decoding autumn phenology: unraveling the link between observation methods and detected environmental cues. Glob. Change Biol. 30, e17231.

Knohl, A., Schulze, E.-D., Kolle, O., Buchmann, N., 2003. Large carbon uptake by an unmanaged 250-year-old deciduous forest in Central Germany. Agric. For. Meteorol. 118, 151–167.

Lanconelli, C., Cappucci, F., Adams, J.S., Gobron, N., 2024. Evaluation of in situ FAPAR measurement protocols using 3D radiative transfer simulations. Remote Sens. 16. https://doi.org/10.3390/rs16234552.

Leblanc, S.G., Chen, J.M., 2001. A practical scheme for correcting multiple scattering effects on optical LAI measurements. Agric. For. Meteorol. 110, 125–139.

Lee, L.X., Whitby, T.G., Munger, J.W., Stonebrook, S.J., Friedl, M.A., 2023. Remote sensing of seasonal variation of LAI and fAPAR in a deciduous broadleaf forest. Agric. For. Meteorol. 333, 109389.

Lerebourg, C., Grousset, R., Vidal, T., Bai, G., Clerici, M., Gobron, N., Dash, J., Bar, S., James, F., Brown, L., 2024. GBOV (Copernicus Ground-Based Observation for Validation) service: latest product and evolutions for EO data Cal/Val. In: EGU General Assembly Conference Abstracts, 10447.

Li, J., Xiao, Z., Sun, R., Song, J., 2023. A method to estimate leaf area index from VIIRS surface reflectance using deep transfer learning. ISPRS J. Photogramm. Remote Sens. 202, 512–527.

Li, W., Fang, H., Wei, S., Weiss, M., Baret, F., 2021. Critical analysis of methods to estimate the fraction of absorbed or intercepted photosynthetically active radiation from ground measurements: application to rice crops. Agric. For. Meteorol. 297, 108273.

Chapter 11 - Fraction of absorbed photosynthetically active radiation. In: Liang, S., Wang, J. (Eds.), 2020. Advanced Remote Sensing, 2nd Edition. Academic Press, pp. 447–476. https://doi.org/10.1016/B978-0-12-815826-5.00011-8.

Lin, W., Yuan, H., Dong, W., Zhang, S., Liu, S., Wei, N., Lu, X., Wei, Z., Hu, Y., Dai, Y., 2023. Reprocessed MODIS version 6.1 leaf area index dataset and its evaluation for land surface and climate modeling. Remote Sens. 15, 1780.

Liu, C., Calders, K., Origo, N., Terryn, L., Adams, J., Gastellu-Etchegorry, J.-P., Wang, Y., Meunier, F., Armston, J., Disney, M., 2024a. Bitemporal radiative transfer modeling using bitemporal 3D-explicit forest reconstruction from terrestrial laser scanning. Remote Sens. 16, 3639.

Liu, J., Cai, Y., Pei, X., Yu, X., 2025. Advances in research and application of techniques for measuring photosynthetically active radiation. Remote Sens. 17, 1765.

Liu, L., Li, Q., Liao, X., Wu, W., 2024b. Bird droppings defects detection in photovoltaic modules based on CA-YOLOv5. Processes 12, 1248.

Loewensteiner, D.A., Bartolo, R.E., Whiteside, T.G., Esparon, A.J., Humphrey, C.L., 2021. Measuring savanna woody cover at scale to inform ecosystem restoration. Ecosphere 12, e03437.

Long, C.N., Shi, Y., 2008. An automated quality assessment and control algorithm for surface radiation measurements. Open Atmos. Sci. J. 2, 23–37.

López-Baeza, E., Velázquez, A., Antolín, C., Bodas, A., Gimeno, J., Saleh, K., Sánchez, M., 2003. The Valencia anchor station, a Cal/Val reference area for largescale low spatial resolution remote sensing missions. In: Proc. 3rd International Conference on Experiences with Automatic Weather Stations, pp. 19–21.

Lozano, I., Alados, I., Sánchez-Hernández, G., Guerrero-Rascado, J.L., Foyo-Moreno, I., 2023a. Improving the estimation of the diffuse component of photosynthetically active radiation (PAR). J. Geophys. Res. Atmospheres 128, e2023JD039256.

Lozano, I.L., Alados, I., Foyo-Moreno, I., 2023b. Analysis of the solar radiation/atmosphere interaction at a Mediterranean site: the role of clouds. Atmospheric Res 296, 107072.

Ma, H., Liang, S., Xiong, C., Wang, Q., Jia, A., 2022. Global land surface 250-m 8-day fraction of absorbed photosynthetically active radiation (FAPAR) product from 2000 to 2020. Earth Syst. Sci. Data Discuss. 2022, 1–22.

Macfarlane, C., Ryu, Y., Ogden, G.N., Sonnentag, O., 2014. Digital canopy photography: exposed and in the raw. Agric. For. Meteorol. 197, 244–253.

Majasalmi, T., Stenberg, P., Rautiainen, M., 2017. Comparison of ground and satellite-based methods for estimating stand-level fPAR in a boreal forest. Agric. For. Meteorol. 232, 422–432.

Martínez, B., Camacho, F., Verger, A., García-Haro, F.J., Gilabert, M., 2013. Intercomparison and quality assessment of MERIS, MODIS and SEVIRI FAPAR

products over the Iberian Peninsula. Int. J. Appl. Earth Obs. Geoinformation 21, 463–476.

McCallum, I., Wagner, W., Schmullius, C., Shvidenko, A., Obersteiner, M., Fritz, S., Nilsson, S., 2010. Comparison of four global FAPAR datasets over Northern Eurasia for the year 2000. Remote Sens. Environ. 114, 941–949. https://doi.org/10.1016/j.rse.2009.12.009.

Mõttus, M., Sulev, M., Baret, F., Lopez-Lozano, R., Reinart, A., 2012. Photosynthetically active radiation: measurement and modeling. Encyclopedia of Sustainability Science and Technology. Springer, pp. 7970–8000.

Myneni, R.B., Hoffman, S., Knyazikhin, Y., Privette, J., Glassy, J., Tian, Y., Wang, Y., Song, X., Zhang, Y., Smith, G., 2002. Global products of vegetation leaf area and fraction absorbed PAR from year one of MODIS data. Remote Sens. Environ. 83, 214–231.

Nestola, E., Sánchez-Zapero, J., Latorre, C., Mazzenga, F., Matteucci, G., Calfapietra, C., Camacho, F., 2017. Validation of PROBA-V GEOV1 and MODIS C5 & C6 FAPAR products in a deciduous beech forest site in Italy. Remote Sens. 9, 126.

Nightingale, J., Boersma, K.F., Muller, J.-P., Compernolle, S., Lambert, J.-C., Blessing, S., Giering, R., Gobron, N., De Smedt, I., Coheur, P., 2018. Quality assurance framework development based on six new ecv data products to enhance user confidence for climate applications. Remote Sens. 10, 1254.

Niro, F., Goryl, P., Dransfeld, S., Boccia, V., Gascon, F., Adams, J., Themann, B., Scifoni, S., Doxani, G., 2021. European Space Agency (ESA) calibration/validation strategy for optical land-imaging satellites and pathway towards interoperability. Remote Sens. 13, 3003.

Origo, N., Calders, K., Nightingale, J., Disney, M., 2017. Influence of levelling technique on the retrieval of canopy structural parameters from digital hemispherical photography. Agric. For. Meteorol. 237, 143–149.

Origo, N.J., 2023. Measuring and modelling fAPAR for satellite product validation (PhD Thesis). UCL (University College London).

Pashiardis, S., Pelengaris, A., Kalogirou, S.A., 2023. Geographical distribution of global radiation and sunshine duration over the island of Cyprus. Appl. Sci. 13, 5422.

Pickett-Heaps, C.A., Canadell, J.G., Briggs, P.R., Gobron, N., Haverd, V., Paget, M.J., Pinty, B., Raupach, M.R., 2014. Evaluation of six satellite-derived fraction of absorbed photosynthetic active radiation (FAPAR) products across the Australian continent. Remote Sens. Environ. 140, 241–256.

Pu, J., Yan, K., Roy, S., Zhu, Z., Rautiainen, M., Knyazikhin, Y., Myneni, R.B., 2023. Sensor-independent LAI/FPAR CDR: reconstructing a global sensor-independent climate data record of MODIS and VIIRS LAI/FPAR from 2000 to 2022. Earth Syst. Sci. Data Discuss. 2023, 1–29.

Putzenlechner, B., Castro, S., Kiese, R., Ludwig, R., Marzahn, P., Sharp, I., Sanchez-Azofeifa, A., 2019a. Validation of Sentinel-2 fAPAR products using ground observations across three forest ecosystems. Remote Sens. Environ. 232, 111310.

Putzenlechner, B., Marzahn, P., Kiese, R., Ludwig, R., Sanchez-Azofeifa, A., 2019b. Assessing the variability and uncertainty of two-flux FAPAR measurements in a conifer-dominated forest. Agric. For. Meteorol. 264, 149–163.

Putzenlechner, B., Marzahn, P., Koal, P., Sánchez-Azofeifa, A., 2022. Fractional vegetation cover derived from UAV and Sentinel-2 imagery as a proxy for in situ FAPAR in a dense mixed-coniferous forest? Remote Sens. 14, 380.

Putzenlechner, B., Marzahn, P., Sanchez-Azofeifa, A., 2020. Accuracy assessment on the number of flux terms needed to estimate in situ fAPAR. Int. J. Appl. Earth Obs. Geoinformation 88, 102061.

Roebeling, R., Bojinski, S., Poli, P., John, V., Schulz, J., 2025. On the determination of GCOS ECV product requirements for climate applications. Bull. Am. Meteorol. Soc. 106, E868–E893.

Rogers, C., Chen, J.M., Croft, H., Gonsamo, A., Luo, X., Bartlett, P., Staebler, R.M., 2021. Daily leaf area index from photosynthetically active radiation for long term records of canopy structure and leaf phenology. Agric. For. Meteorol. 304, 108407.

Sanchez-Azofeifa, A., Sharp, I., Green, P.D., Nightingale, J., 2022. Calibration of co-located identical PAR sensors using wireless sensor networks and characterization of the in situ fPAR variability in a tropical dry forest. Remote Sens. 14, 2752.

Sánchez-Zapero, J., Martínez-Sánchez, E., Camacho, F., Wang, Z., Carrer, D., Schaaf, C., García-Haro, F.J., Nickeson, J., Cosh, M., 2023. Surface ALbedo VALidation (SALVAL) platform: towards CEOS LPV validation stage 4—application to three global albedo climate data records. Remote Sens. 15, 1081.

Sellers, P.J., Dickinson, R., Randall, D., Betts, A.K., Hall, F.G., Berry, J.A., Collatz, G., Denning, A., Mooney, H.A., Nobre, C.A., 1997. Modeling the exchanges of energy, water, and carbon between continents and the atmosphere. Science 275, 502–509.

Senna, M.C., Costa, M.H., Shimabukuro, Y.E., 2005. Fraction of photosynthetically active radiation absorbed by Amazon tropical forest: a comparison of field measurements, modeling, and remote sensing. J. Geophys. Res. Biogeosciences 110.

Steinberg, D.C., Goetz, S.J., Hyer, E.J., 2006. Validation of MODIS F/sub PAR/products in boreal forests of Alaska. IEEE Trans. Geosci. Remote Sens. 44, 1818–1828.

Tamrakar, R., Rayment, M.B., Moyano, F., Mund, M., Knohl, A., 2018. Implications of structural diversity for seasonal and annual carbon dioxide fluxes in two temperate deciduous forests. Agric. For. Meteorol. 263, 465–476.

Tao, X., Liang, S., Wang, D., 2015. Assessment of five global satellite products of fraction of absorbed photosynthetically active radiation: intercomparison and direct validation against ground-based data. Remote Sens. Environ. 163, 270–285.

Thiel, C., Mueller, M.M., Epple, L., Thau, C., Hese, S., Voltersen, M., Henkel, A., 2020. Uas imagery-based mapping of coarse wood debris in a natural deciduous forest in central germany (hainich national park). Remote Sens. 12, 3293.

Vedurmudi, A.P., Miličević, K., Kok, G., Yong, B.X., Xu, L., Zheng, G., Brintrup, A., Gruber, M., Tabandeh, S., Zaidan, M.A., 2025. Automation in sensor network metrology: an overview of methods and their implementations. Meas. Sens., 101799

Wan, L., Ryu, Y., Dechant, B., Hwang, Y., Feng, H., Kang, Y., Jeong, S., Lee, J., Choi, C., Bae, J., 2024. Correcting confounding canopy structure, biochemistry and soil background effects improves leaf area index estimates across diverse ecosystems from Sentinel-2 imagery. Remote Sens. Environ. 309, 114224.

Wang, Y., Xie, D., Liu, S., Hu, R., Li, Y., Yan, G., 2016. Scaling of FAPAR from the field to the Satellite. Remote Sens. 8, 310.

Widlowski, J.-L., 2010. On the bias of instantaneous FAPAR estimates in open-canopy forests. Agric. For. Meteorol. 150, 1501–1522.

Wojnowski, W., Wei, S., Li, W., Yin, T., Li, X.-X., Ow, G.L.F., Mohd Yusof, M.L., Whittle, A.J., 2021. Comparison of absorbed and intercepted fractions of PAR for individual trees based on radiative transfer model simulations. Remote Sens. 13, 1069.

Xia, L., Gong, S., Li, L., Zhang, H., Wen, J., Han, L., Xin, X., Yu, S., Liu, Q., 2025. A comprehensive evaluation of global fraction of absorbed photosynthetically active radiation (FAPAR) products of MODIS, GLASS, and GEO over China. IEEE J. Sel. Top. Appl. Earth Obs. Remote Sens.

Xiao, Z., Liang, S., Sun, R., 2018. Evaluation of three long time series for global fraction of absorbed photosynthetically active radiation (FAPAR) products. IEEE Trans. Geosci. Remote Sens. 56, 5509–5524.

Xiao, Z., Liang, S., Sun, R., Wang, J., Jiang, B., 2015. Estimating the fraction of absorbed photosynthetically active radiation from the MODIS data based GLASS leaf area index product. Remote Sens. Environ. 171, 105–117. https://doi.org/10.1016/j.rse.2015.10.016.

Yan, K., Park, T., Yan, G., Liu, Z., Yang, B., Chen, C., Nemani, R.R., Knyazikhin, Y., Myneni, R.B., 2016. Evaluation of MODIS LAI/FPAR product collection 6. Part 2: validation and intercomparison. Remote Sens. 8, 460.

Yan, K., Yu, X., Liu, J., Wang, J., Chen, X., Pu, J., Weiss, M., Myneni, R.B., 2025. HiQ-FPAR: a high-quality and value-added MODIS Global FPAR product from 2000 to 2023. Sci. Data 12, 72.

Yu, X., Wu, Z., Jiang, W., Guo, X., 2015. Predicting daily photosynthetically active radiation from global solar radiation in the contiguous United States. Energy Convers. Manag. 89, 71–82.

Zemp, M., Chao, Q., Han Dolman, A.J., Herold, M., Krug, T., Speich, S., Suda, K., Thorne, P., Yu, W., 2022. Gcos 2022 implementation plan.

Zhang, Q., Cheng, Y.-B., Lyapustin, A.I., Wang, Y., Gao, F., Suyker, A., Verma, S., Middleton, E.M., 2014. Estimation of crop gross primary production (GPP): fAPARchl versus MOD15A2 FPAR. Remote Sens. Environ. 153, 1–6.

Zhang, X., Jin, H., Zhao, W., Yin, G., Xie, X., Fan, J., 2024. Assessment of satellite-derived FAPAR products with different spatial resolutions for gross primary productivity estimation. IEEE J. Sel. Top. Appl. Earth Obs. Remote Sens.

Zhang, Y., Fang, H., Hu, Z., Wang, Y., Li, S., Wu, G., 2025. Validation of global moderate-resolution FAPAR products over boreal forests in North America using harmonized landsat and sentinel-2 data. Remote Sens 17, 2658.

Zhang, Y., Fang, H., Wang, Y., Li, S., 2021. Variation of intra-daily instantaneous FAPAR estimated from the geostationary Himawari-8 AHI data. Agric. For. Meteorol. 307, 108535.

Zhang, Y., Hu, Z., Fang, H., Gao, X., Wang, J., Wu, G., 2023. Estimation of daily FAPAR from MODIS instantaneous observations at forest sites. Agric. For. Meteorol. 331, 109336.

Zhao, L., Liu, Z., Xu, S., He, X., Ni, Z., Zhao, H., Ren, S., 2018. Retrieving the diurnal FPAR of a maize canopy from the jointing stage to the tasseling stage with vegetation indices under different water stresses and light conditions. Sensors 18, 3965.

Zhao, W., Zhu, Z., Cao, S., Li, M., Zha, J., Pu, J., Myneni, R.B., 2024. A global dataset of the fraction of absorbed photosynthetically active radiation for 1982–2022. Sci. Data 11, 707.

Zheng, Y., Xiao, Z., Li, J., Yang, H., Song, J., 2022. Evaluation of global fraction of absorbed photosynthetically active radiation (FAPAR) products at 500 m spatial resolution. Remote Sens. 14, 3304.

Zhu, Z., Bi, J., Pan, Y., Ganguly, S., Anav, A., Xu, L., Samanta, A., Piao, S., Nemani, R.R., Myneni, R.B., 2013. Global data sets of vegetation leaf area index (LAI) 3g and fraction of photosynthetically active radiation (FPAR) 3g derived from global inventory modeling and mapping studies (GIMMS) normalized difference vegetation index (NDVI3g) for the period 1981 to 2011. Remote Sens. 5, 927–948.